2D Material Integration with Integrated Photonics: Waveguides, Micro-ring Resonators and Photodetectors

by Chandraman Sadanand Patil

B.E. in Electronics Engineering, June 2017, Vidyalankar Institute of Technology, University of Mumbai

A Thesis submitted to

The School of Engineering and Applied Science
of The George Washington University
in partial fulfillment of the requirements
for the degree of Master of Science

May 19, 2019

Thesis directed by

Volker J. Sorger
Associate Professor of Engineering and Applied Science

Dedication

This thesis is dedicated to my father and mother, who taught me that hard work and complete devotion towards achieving your goals provides the true path to success. It is also dedicated to my brother and friends, whose moral support, suggestions and blessings strengthened my efforts.

Acknowledgments

I would like to express my gratitude to Prof. Volker J. Sorger for finding me capable to become a researcher as a master student, and for providing phenomenal research opportunities, mentoring and guiding me along this journey. Also, I am thankful to the whole research team in Orthogonal-Physics-Enabled-Nanophotonic (OPEN) Lab at The George Washington University. Additionally, I would like to thank all the professors in The George Washington University who have helped me in my learning and acclimation to the United States. Lastly, my thanks go to my family for their unconditional love, support, and understanding.

Abstract of Thesis

2D Material Integration with Integrated Photonics:
Waveguides, Micro-ring Resonators and Photodetectors

This thesis reports research that exploits the strong light-matter interaction by the integration of the two-dimensional (2D) materials like transition metal dichalcogenides (TMDCs), for example, Molybdenum Ditelluride ($MoTe_2$), Molybdenum Disulfide (MoS_2) and Hexagonal Boron Nitride (hBN), with photonic devices like waveguides and micro-ring resonators (MRRs). The TMDC materials play a significant role in changing the effective refractive index (n_g) and light absorption loss (κ) of the photonic devices, which can be engineered for development and advancement of optoelectronic devices and applications.

The first study of the thesis was to experimentally characterize the effect of heterogeneous integration of TMDCs with silicon integrated photonic devices at 1550 nm wavelength. The experiments performed shows the change in refractive index and optical loss with change in the length and thickness of the TMDCs covering the devices (waveguides and micro-ring resonators).

The thesis reports research that proceeded with designing and fabrication of photodetectors by using $MoTe_2$ as the active material integrated with waveguides and micro-ring resonators. The material, after integration, was probed with two terminal transport measurements using electrical contacts to analyze the responsivity and dark

current of the device. The design of contact pads was based on the image mapping of the TMDC flake on the device.

Lastly, the thesis also covers the fabrication of waveguides and grating couplers using silicon nitride. The development of this platform is to design devices, which can operate in the visible spectrum (here at □ = 640 nm) and observe the effect of TMDCs at the excitonic wavelength of the material. The linear grating couplers were designed to enable coupling light from a free space Gaussian laser beam (640 nm) into the waveguides.

Furthermore, the thesis also discusses the methodology used for integrating the TMDCs with the photonic devices, and all the optimizations made to the experimental setup for making it possible. The tools and services utilized, and challenges faced throughout the processes like 2D material transfer, Nanofabrication processes, and tools, availability of resources and official processing times for requests of orders making this research success, are briefly addressed at the end.

Table of Contents

Dedication ii

Acknowledgments iii

Abstract of Thesis iv

Table of Contents vi

List of Figures vii

List of Tables xii

1. Introduction 1

2. Heterogeneous Integration of MoS_2 Layers in Silicon Photonics for Optical Loss and Coupling Tunability Analysis 5

2.1 Introduction 5

2.2 Methods 6

2.3 Results & Discussion 9

2.4 Conclusion 16

3. $MoTe_2$ integrated Photodetectors 17

3.1 Introduction 17

3.2 Methodology 18

3.3 Results and Discussion 23

3.4 Conclusion 25

4. Silicon Nitride-based Platform for Photonic Devices 26

4.1 Introduction 26

4.2 Methodology 28

4.3 Results and discussion 32

4.4 Conclusion 34

5. Challenges 36

6. Conclusion 38

Appendix A 45

1. 2D Printer Modifications and Optimizations 45

1.1 Change in working distance 46

1.2 Change in the motion of the needle 47

1.3 Temperature-dependent transfers 49

List of Figures

Figure 1 Optical microscope image of process steps (a) Micro-ring resonators on SOI chip (Applied Nanotools INC.), (b) Patterned opening to transfer 2D materials on top of the Si MRR, (c) 2D Printer setup for TMDC flake transfer on the Si MRR (d) MoS_2 flakes transferred on targeted device area. 9

Figure 2 MoS2 loaded micro-ring resonator (MRR) (a) schematic (b) optical microscope image of an MRR (R= 40 μm & W= 500 nm) covered by two monolayer MoS_2 flakes with coverage lengths (l_1 *and* l_2) precisely transferred using our developed 2D printer technique(*2D material printer.*) (c) Transmission output before and after the transfer of monolayer MoS_2 showing improvement of coupling efficiency. (d) & (e) optical microscope image and AFM image of an MRR showing a multi-layer MoS_2 flake with coverage length 22 μm and thickness of 30 nm, respectively. (f) Transmission output before and after the two steps of transfer of multilayer MoS_2 flakes which display a gradual increase of visibility suggesting the improvement of coupling efficiency as it brings the device close to the critically coupled regime after the transfer of the TMDs layer (Maiti et al., 2019). 10

Figure 3 MoS2 loaded Linear waveguides (a) optical microscope image of the waveguide with an opening (400 μm x 100 μm) for TMDC transfer to keep all physical parameters unchanged during the optical measurement. (b) & (c) optical microscope image of waveguide covered by a monolayer CVD grown and a multilayer exfoliated flake with coverage length 10 μm and 50 μm, respectively. (d) Optical loss output as a function of monolayer coverage length originates

mainly due to the edge scattering effect. The propagation loss ($\alpha_{TMDC\text{-}Si}$) for a TMDC-covered portion of the ring is found to be 0.012 dB/μm using cutback measurement. (e) Tunability of round-trip transmission coefficients explains the coupling improvement as a function of coverage length for four different thickness values (Maiti et al., 2019). 11

Figure 4 Mode profile (electric |E|-field) by Eigenmode analysis for the portion of the ring with MoS_2 transferred flakes (a) 20 nm and (b) 50 nm thick (Scale bar 200 nm). Variation of Resonance shift ($\Delta\boldsymbol{\lambda}$) and effective index change ($\Delta\boldsymbol{neff}$) extracted from (c) as a function of MoS_2 coverage length and (d) thickness, which is fully corroborated by a numerical simulation study. 14

Figure 5 Few-layered $MoTe_2$ Photodetector on Si MRR (a) Conceptual schematic design of $MoTe_2$ photodetector fabricated on a Si MRR on SOI substrate (b) Optical microscopic image of the fabricated $MoTe_2$ photodetector. $MoTe_2$ flake was transferred on a Si MRR with two metal contacts of 45 nm gold on a 5 nm titanium layer (Ti/Au) forming the electrical contacts to the active material. A laser light (1550 nm) signal was fiber coupled into the device via grating couplers and coupled into the device by silicon MRR. 17

Figure 6 Position mapping of MoTe2 flake for contact pad designing (a) Optical image captured at 20x magnification after PMMA (~300nm) layer was coated (b) The image was converted to 24-bit Bitmap format using Microsoft Paint software maintaining the size of image (c) The image was scaled to the device size in the CAD file to determine the exact position of the $MoTe_2$ flake (d) The contact pads

and probes were designed based on the size and shape of the flake observed from the image 20

Figure 7 Fabrication of photodetector using MoTe2 as the active material. The pre-baking process at Step 2 is very important to remove humidity as it reduces the adhesion of the flake with the substrate and the device. The humidity forms small bubbles under the flake during the rest of the steps due to high temperatures involved in the processes affecting the contact with the Si MRR. The spin speed while coating PMMA in Step 3 and Step 7 was reduced from 4000rpm to 1500 rpm to avoid the flakes from moving away from the transferred position due to the viscosity of the PMMA. 22

Figure 8 $MoTe_2$ photodetector analysis (a) Optical microscopic image of the fabricated $MoTe_2$ photodetector (b) Magnified SEM image of the device showing the $MoTe_2$ flake with two metal contacts above the Si MRR (c) Logarithm-scale I−V curves without light (black line) and with light (red line) (d) Measured output transmission power (blue line) from the output grating coupler of Si MRR and photocurrent (red line) from the two terminals of the device with respect to wavelength showing the maximum peaks. 24

Figure 9 Design of waveguide and grating coupler: The duty cycle of the grating couplers was 50% and the period was 1500 nm. The width of the waveguide is 500nm and the length is 100 um. The depth of the grating coupler is ~215 nm. 29

Figure 10 Silicon Nitride waveguides and grating couplers fabrication process The current and dose values were optimized for over-dose and under-dose effects on the negative photoresist. The electron beam lithography speed was reduced for

patterning the grating couplers for better resolution and control over exposure time. A lateral etch of 10-15 nm was observed in Step 5 reducing the effective size of the waveguide to ~470-480 nm and period of ~1520-1530 nm. The duty cycle was shifted to ~53%. The devices working even with these variations but with lower efficiency due to loss caused majorly by reflection and scattering. 30

Figure 11 SEM images of damage to structures during development and rinsing of the sample during fabrication 31

Figure 12 Image processing using MATLAB for the integration of intensities 32

Figure 13 SEM of Grating Coupler (a)Vertical edge of Grating coupler. The sample was placed at ~90 degrees on the sample holder of the SEM machine. The moving stage of the SEM was titled by an angle of 1.68 degrees to capture the side view of the grating coupler (b)Top view of the grating coupler with a tilt of 30 degrees to observe the smoothness of the walls by using SEM. 33

Figure 14 Edge roughness improvement (a) Before optimizations the sidewall roughness was ~5 nm - 6 nm (b) After Optimizations the sidewall roughness was < ~4 nm. The roughness was calculated using a MATLAB program but for accurate measurements a Focused Ion Beam (FIB) SEM is required. 34

Figure 15 Cracking of 2D material flakes 47

Figure 16 Glass slide frame for holding PDMS and reducing the working distance 47

Figure 17 Micro stamper holder fixed on a stationary platform attached by permanent magnets 48

Figure 18 Linear xyz-direction micro-step control stage with the needle holding clip 49

Figure 19 Thermal hot plate introduced in 2D printer 50

Figure 20 Temperature dependent transfer using a modified 2D printer 51

List of Tables

Table 1 Losses associated with 2D materials integrated with Silicon photonics platform 13

Table 2 Silicon versus Silicon Nitride properties for optical applications (Baets et al., 2016/03/20) 27

1. Introduction

The two-dimensional (2D) materials began to be extensively involved in research after the first isolation of very thin atomic layer of graphene was made possible (Amin et al., 2018; Freitag, 2008; Geim & Novoselov, 2007; Morozov et al., 2008). The 2D materials like graphene and other materials can be intensely used for integration with various optoelectronic, quantum and electrical devices. Various applications based on electronics, valleytronics, catalysis, and biosensing can be built by exploring the characteristics and unique properties of these materials. The 2D materials can be utilized as single atomic layers to few layers up to bulk. The materials can be in the elemental forms like graphene and phosphorous, mixed layered materials like transition metal dichalcogenides (TMDCs), van der Waals heterostructures and MXenes (2D materials.2016). All these materials possess unique properties like high carrier mobilities, superconductivity, mechanical flexibility, thermal conductivity, and importantly high optical adsorption plus change in optical index and loss.

Transition metal dichalcogenides are a family of materials represented generally as MX_2, where M represents a transition metal (W, Re, Mo) and X represents a chalcogen (Te, S or Se). TMDCs can be used to build atomically thin heterostructures for integration with devices (Mak, Lee, Hone, Shan, & Heinz, 2010; Manzeli, Ovchinnikov, Pasquier, Yazyev, & Kis, 2017). The 2D materials can be easily integrated with silicon and CMOS platforms without any need of lattice matching (Ma et al., 2018). This thesis deals with characterization and study of the effects of TMDCs on photonic devices to develop passive devices and active tunable devices for optoelectronic applications.

The field of photonics deals with the study of generation, detection, and manipulation of light (Yeh, 2012). Due to the difference in the size of a photon (or light) and an atom, the strength of the interaction is extremely weak. Therefore, an interface between them has to be developed that creates a strong light-matter interaction (Xiao et al., 2012). These interactions govern the linear and especially nonlinear optical properties of the materials (Lienau, Noginov, & Lončar, 2014). It is important to enhance the light-matter interaction for building passive and active tunable devices, which can widen the possibilities of new applications and improve the development in the current photonic platforms. TMDCs in the form of monolayers show an indirect to direct bandgap transition, with a direct bandgap ranging from 1.57 to 2.2 eV for various TMDC materials (Ma et al., 2018; Sun, Martinez, & Wang, 2016). At near 10% bandgap resonances, the optical absorption in monolayer semiconducting TMDCs is very strong. Studies from the literature show that the excitonic transitions in semiconductor TMDCs exhibit dominance for these optical resonances. The exciton binding energy reported is hundreds of meV as an effect of the enhanced electron-electron interactions in 2D monolayers being one of the inherent properties (Cao, Stoumpos, Farha, Hupp, & Kanatzidis, 2015; Sun et al., 2016). Therefore, it is understood that the TMDCs will be strong optical absorbers in the form of thin layers when operated at or near bandgap wavelengths. An extensive study has been performed in measuring the refractive index of MoS_2 in the range of 400 nm to 750 nm (Zhang et al., 2015). The thesis focuses on studying the effect of the TMDCs on the integrated silicon photonic (SiP) platform at 1550nm wavelength also called a telecommunication wavelength used in commercial optical applications.

Silicon photonics (SiP) is a widely used platform for integrated devices for applications like data-communication, photonic processes, signals and systems, and sensing and telecommunication (Miller, 2017). Research reported in the thesis advances with the fabrication of passive devices by integrating MoS_2 material on Silicon waveguides and micro-ring resonators. The experiment and fabrication processes were performed to understand the change in effective refractive index and loss in the devices due to MoS_2. The length and thickness of the MoS_2 were varied such that the coverage length can be changed leading to a differences in key parameters (Maiti et al., 2019). This technique was developed to characterize the properties of TMDCs (here MoS_2) for its effect in photonic devices. It can be applied to study of more such materials.

After studying the characteristics of MoS_2, it was observed that a reasonable shift in the index can be achieved with negligible or minimal losses after integration of TMDCs and SiP due to operation at far away from the exciton range leading to negligible absorption of light. The bandgap of MoS_2 lies in the visible spectrum of light, and the operating wavelength (1550 nm) used in the experiment is far away from it. It is expected that the optical absorption far away from the excitonic range (near bandgap) is negligible or minimal. The experimental results thus helped to verify and quantify these effects.

The research moved ahead with an aim to study active devices like photodetectors and modulators using TMDCs within active devices. The photodetector devices convert the optical energy to electrical energy by generating charge carriers in the material due to the absorption of light. The photodetectors were designed and fabricated using $MoTe_2$ as the active material. $MoTe_2$, among the other TMDCs whose exciton wavelength lies in the visible spectrum, has a bandgap (1.0 eV) in the near infrared. The active material in

the photodetectors was contacted with titanium and gold pads (Ti/Au:5 nm/45 nm) for electrical probing, providing better charge conduction and low contact resistance for the device. The photodetector devices were optimized for high responsivity and low dark current. They were operated at 1550 nm i.e. far away from its exciton wavelength. Both parameters are key aspects of photodetectors to achieve better absorption and high-speed performance (Ma et al., 2018).

As noted, the TMDCs were studied with all the experiments by operating far away from the exciton wavelength of the materials in SiP. To explore the impact of TMDCs on optical devices it is important to perform a similar study at exciton wavelength of the TMDCs, where the resonance and absorption will be very high. The exciton wavelengths of TMDCs belong in the range from visible range to near-infrared (NIR) spectrum. It is highly desirable to design devices on a photonics platform operating in this range. But, the SiP platform cannot be used for the visible spectrum operations since the material bandgap blocks (i.e. absorbs) these wavelengths. Therefore, a new platform development using silicon nitride for visible spectrum optical operations was fabricated. Silicon Nitride is transparent for frequencies in visible spectrum due to his larger bandgap, which also enables lower optical absorption since the carrier density is lower compared to Silicon.

2. Heterogeneous Integration of MoS_2 Layers in Silicon Photonics for Optical Loss and Coupling Tunability Analysis

2.1 Introduction

Molybdenum disulfide (MoS2) is possessed with unique electrical and optoelectronic properties such as high mobility at 300K temperature, bandgap tunability, high switching characteristics, and high exciton binding energies (Kis, Giacometti, Brivio, Radenovic, & Radisavljevic, 2011; Maiti et al., 2019; Splendiani et al., 2010; Ugeda et al., 2014)(Kis, Giacometti, Brivio, Radenovic, & Radisavljevic, 2011; Maiti et al., 2019; Splendiani et al., 2010; Ugeda et al., 2014). Due to quantum confinement, the few-layer MoS_2 with an indirect bandgap of ~1.2 eV traverses to a direct bandgap of ~1.8 eV in its monolayer form (Ugeda et al., 2014). This material is studied here to study the impact of optical absorption and index-shift when heterogeneously integrated with SiP waveguides and micro-ring resonator (MRR). The spectral distance of each TMDC's exciton is relatively different from the waveguide operating wavelength (here, $\lambda = 1550$ nm. This shows variation in impact on the same operating wavelength as the real and imaginary part of the optical index reduce far away from the exciton resonance (Maiti et al., 2019).

Silicon photonics has opened doors for a wide range of applications in optoelectronics for telecommunication (Miller, 2017). The opt-electronic device functionalities and operating ranges are limited in silicon photonics due to its indirect bandgap and weak electro-optic properties. The 2D materials can be easily integrated with photonic chip due to its strong van der Waals force. This enhances the light-matter interaction thus increasing the possibilities of using its electrical and optical properties for the

development of optoelectronics devices (Bie et al., 2017; Lee et al., 2017; Ye et al., 2015; Youngblood, Chen, Koester, & Li, 2015).

A comparative study for determination of the change in effective refractive index and optical loss is done by heterogeneous integration of TMDC on silicon waveguide and micro-ring resonator (MRR) by varying the coverage length and thickness of MoS2 at 1550 nm wavelength. The effect of MRR-to-waveguide coupling has been mapped out in terms of resonance shift as a function of monolayer coverage analyzing the loss induced by monolayer MoS2 which is found to be about 0.012 dB/μm. We obtain a resonance shift per unit waveguide coverage length of 0.064 nm/μm as a function of thickness which matches our numerical results well. Together these experimental studies of integrating MoS2 with Silicon photonics shows an induced negligible loss, but relatively strong index-tuning potential thus paving the way for future studies of active optoelectronic device technology (Maiti et al., 2019).

2.2 Methods

The integration of TMDCs (MoS_2) was performed on taped out SiP chips (APPLIED NANOTOOLS INC.). It is crucial to observe the influence of the 2D materials and avoiding any other factors affecting the output. The coupling efficiency of the grating couplers was enhanced by adding a cladding layer of polymer to the taped-out chip. A uniformly coated layer of polymethyl methacrylate (PMMA) (~300 nm) was used as a cladding for the improvement of coupling efficiencies of the grating couplers (GC). The PMMA layer was coated using spin coating at 1500 rpm speed and the sample was post-

baked at 180^{o}C for two minutes. The 2D materials cannot be transferred over the cladding layer on the devices as the light-matter interaction will be reduced and the output will be influenced by both the 2D material and the PMMA layer. It is important to have immediate contact between the 2D material and the device. For the transfer of 2D materials, a rectangular opening was patterned using electron beam lithography in the target region where the flakes are to be transferred using the 2D printer tool (Hemnani et al., 2018). The PMMA coated was used as a mask. The complete outcome after each process step can be seen in Figure 1.

We can certainly estimate from the common understanding that the thickness of the MoS_2 flakes will determine the extent of interaction with the device. Among various methods of obtaining multi-layer and monolayer TMDCs, the scotch tape exfoliation technique was used to obtain few-layer MoS_2 flakes and was transferred using the 2D printing tool on the devices (Hemnani et al., 2018). The monolayer MoS_2 flakes were obtained by growing the layer on silicon-on-insulator (SOI) substrate by chemical vapor deposition (CVD) process (Gang Hee Han et al., 2015; Kim et al., 2011). These monolayer flakes were transferred on a thin PDMS substrate by wet etching technique using KOH followed by the same 2D printer transfer method performed for few-layer flakes. After the transfer is complete, the devices are tested for their optical transmission and spectral shift again to determine the effect caused by the TMDCs layer as a function of coverage length and thickness on the waveguide and MRR. The experimental setup for measuring the hybrid TMDC-Si devices consists of a tunable laser source (Agilent 8164B) and a broadband source (AEDFA-PA-30-B-FA) from where light is injected into the grating coupler optimized for the TM mode propagation in the waveguide. The light

output from the MRR is coupled to the output fiber by a similar grating coupler and detected by a detector or an optical spectral analyzer (OSA202). The fundamental modes of the waveguide which integrate the MoS_2 layer of different thickness are found from the finite element method (FEM) simulations using the mode analysis tool in COMSOL Multiphysics (Maiti et al., 2019).

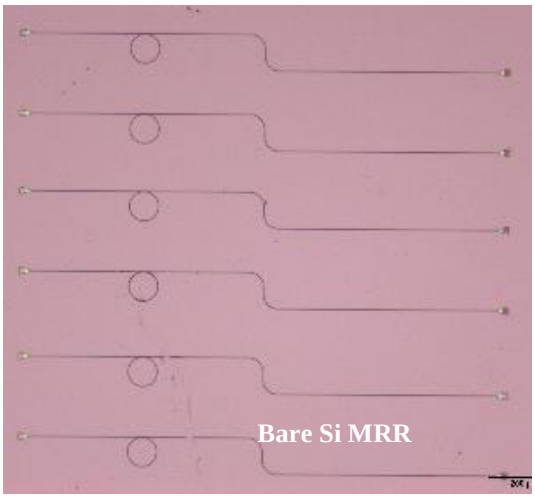

(a)

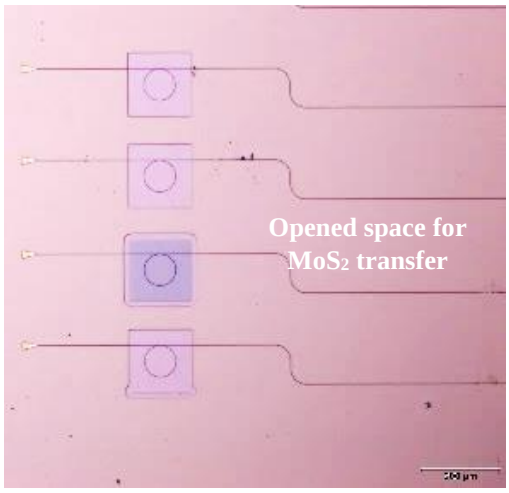

(b)

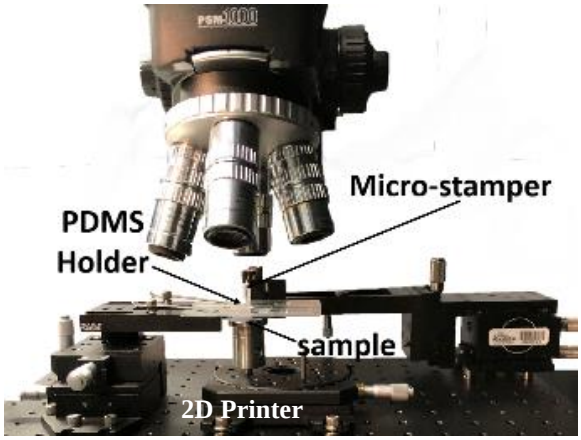

(b)

(d)

Figure 1 Optical microscope image of process steps (a) Micro-ring resonators on SOI chip (Applied Nanotools INC.), (b) Patterned opening to transfer 2D materials on top of the Si MRR, (c) 2D Printer setup for TMDC flake transfer on the Si MRR (d) MoS_2 flakes transferred on targeted device area.

2.3 Results & Discussion

The excitons dominate the optical properties of TMDCs materials. They are bound electron-hole pairs with strong binding energy due to quantum confinement and weak screening of the Coulomb interaction. We investigated the impact on loss and the effective mode index of the Si waveguide operating at hundreds of nanometers away from the excitonic transition of MoS_2 (A exciton ~1.88eV and B Exciton ~2.06eV) (Maiti et al., 2019; Splendiani et al., 2010). We anticipate a minimal loss, with meaningful index changes upon heterogeneous integration. The TMDCs are not electrically driven for any modulation or biasing. The passive impact on the modes index and on MRR shows that design of TMDC-Si hybrid devices, such as phase modulators, is possible (Datta et al., 2018/05/13; Ding et al., 2015; Phare, Daniel Lee, Cardenas, & Lipson, 2015). A study of measuring the resonance shift in the MRR's

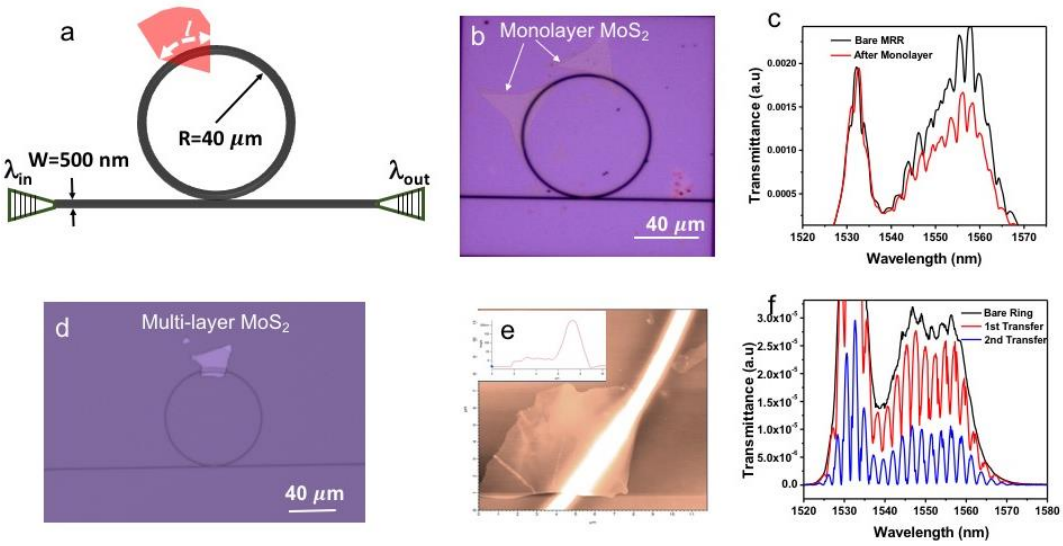

Figure 2 MoS2 loaded micro-ring resonator (MRR) (a) schematic (b) optical microscope image of an MRR (R= 40 μm & W= 500 nm) covered by two monolayer MoS_2 flakes with coverage lengths (l_1 *and* l_2) precisely transferred using our developed 2D printer technique(*2D material printer.*) (c) Transmission output before and after the transfer of monolayer MoS_2 showing improvement of coupling efficiency. (d) & (e) optical microscope image and AFM image of an MRR showing a multi-layer MoS_2 flake with coverage length 22 μm and thickness of 30 nm, respectively. (f) Transmission output before and after the two steps of transfer of multilayer MoS_2 flakes which display a gradual increase of visibility suggesting the improvement of coupling efficiency as it brings the device close to the critically coupled regime after the transfer of the TMDs layer (Maiti et al., 2019).

resonance before and after integration of MoS_2 was performed as shown in Figure 2.

The shift in MRR resonance from the over-coupled regime to the critically-coupled regime improves the coupling. The quality factor of the MRR decreased as the flake thickness increased, leading to a gradual increase in optical loss. This mainly is caused by the scattering effect due to the small impedance mismatch between uncovered and MoS_2 covered regions of the ring.

The fundamental effect of this device is the variation in coupling leading to change in MRR's resonance. This variation in resonance is directly proportional and can be controlled to the variation in coverage length and thickness of the TMDC flakes. It is crucial to find the coupling coefficients, which relates the round-trip transmission

coefficients (a) as a function of variation in the coverage length of the flakes. The transmission, T, from an all-pass MRR is given by,

$$T_n = \frac{a^2 + r^2 - 2ar * cos\varphi}{1 + r^2 a^2 - 2ar * cos\varphi} \quad (1)$$

where φ is the round-trip phase shift, r is the self-coupling coefficient and a is round-trip transmission coefficient related to the power attenuation coefficients by,

$$a^2 = \exp\left(-\alpha_{Si}(2\pi R - l)\right) * \exp(-\alpha_{TMD-Si} * l) \quad (2)$$

where l = TMD coverage length, R is the radius of MRR, α_{Si} and $\alpha_{TMD\text{-}Si}$ are the linear propagation losses for Si waveguide and the TMD-transferred portion of the Si waveguide in the ring, respectively (Maiti et al., 2019). The cutback method was performed to quantify the propagation loss by integrating mono-few layers of MoS_2

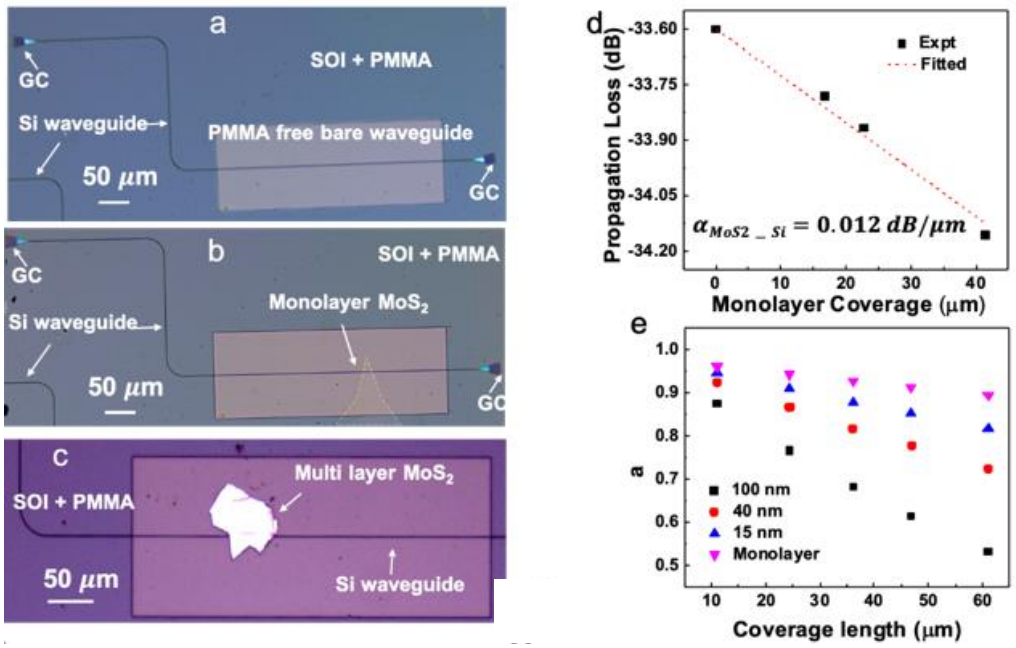

Figure 3 MoS2 loaded Linear waveguides (a) optical microscope image of the waveguide with an opening (400 μm x 100 μm) for TMDC transfer to keep all physical parameters unchanged during the

optical measurement. (b) & (c) optical microscope image of waveguide covered by a monolayer CVD grown and a multilayer exfoliated flake with coverage length 10 μm and 50 μm, respectively. (d) Optical loss output as a function of monolayer coverage length originates mainly due to the edge scattering effect. The propagation loss ($\alpha_{TMDC\text{-}Si}$) for a TMDC-covered portion of the ring is found to be 0.012 dB/μm using cutback measurement. (e) Tunability of round-trip transmission coefficients explains the coupling improvement as a function of coverage length for four different thickness values (Maiti et al., 2019).

on linear waveguides of different lengths and measure the relative transmission Figure 3**Error! Reference source not found.** (b) and (c). The propagation losses obtained from the linear fit are 0.008 dB/μm, 0.012 dB/μm in Figure 3 (d), and 0.04 dB/μm, respectively for Si, monolayer and multi-layer flakes. The excess loss induced by MoS_2 was determined by subtracting the loss of bare Si device from the loss obtained in a hybrid structure, resulting in 0.004 dB/μm and 0.032 dB/μm, respectively for monolayer and multilayer flakes (Maiti et al., 2019).

The loss can be attributed to a combination of absorption and scattering effect of the flake edges. Since the propagation wavelength through the waveguide is well below the bandgap of MoS_2 (1.2-1.8 eV), the losses due to absorption are negligible. Hence, to get more insights, we plot round trip transmission loss for four different thickness values, inserting the propagation loss in Eq. (2) Figure 3 (e). The plot displays the variation of *a* from 0.88 to 0.52 as a function of coverage length for multilayer flakes (~100 nm) and from 0.96 to 0.90 for monolayer flakes, respectively. The result explains the improvement of visibility inducing the transition from over-coupled to towards critically-coupled regime since $a = 1$ is the zero-loss condition of the ring.

Materials	Thickness	Band gap (ev)	Loss (dB/um)	Ref.
Graphene-Si waveguide	Monolayer	Zero	0.1	(Ding et al., 2015)
Black Phosphorous	11nm	~1.5	0.2	(Youngblood et al., 2015)

Black Phosphorous	100nm	~0.3	3.34	(Youngblood et al., 2015)
$MoTe_2$-Si waveguide	Multi-layer (~50 nm)	~0.9	0.4	(Maiti et al., 2018)
MoS_2-Si waveguide	Multi-layer (~30-40 nm)	~1.3	0.037	This work
MoS_2-Si waveguide	Monolayer	~1.8	0.012	This work

Table 1 Losses associated with 2D materials integrated with Silicon photonics platform

Hence, the loss of tunability in MRRs can be manipulated by controlling the coverage length and thickness. We conclude that for a given device, one can determine the coverage length and thickness by configuring the device at a critically coupled condition for optimized light-matter-interaction (Maiti et al., 2018). It is evident from Figure 3(e) that the loss increases as a function of thickness due to an increase in surface roughness. The root-mean-square (rms) roughness of Si waveguide is 1.3±0.6 nm. As a result, a monolayer MoS_2 flake on waveguide (rms roughness: 0.8±0.2 nm) has a much rougher surface compared with the one on SiO_2 (rms roughness: 0.20±.07 nm). For the multilayer flakes, the surface roughness of underlying substrate does not play a significant role since the rms roughness for 40 nm MoS_2 flake is 3.5±0.9 and 3.7±1.3 nm on both SiO_2 and Si waveguide, respectively.

Si-based MRRs provide a compact and ultra-sensitive platform for detection of an unknown analyte for various applications (Tsigaridas, 2017; White & Fan, 2008). Here, the detection mechanism is mostly based on the change of the refractive index in the top-cladding of the MRR. This change can be sensed by the evanescent tail of the propagating optical mode governed by the effective mode index(n_{eff}) and can be translated into resonance shift ($\Delta\lambda$). We observe the resonance shift of 1.5 nm upon ithe

ncrease of monolayer coverage length from 10 to 60 μm Figure 4(c) shows ma onotonic red shift which can be explained as follows:

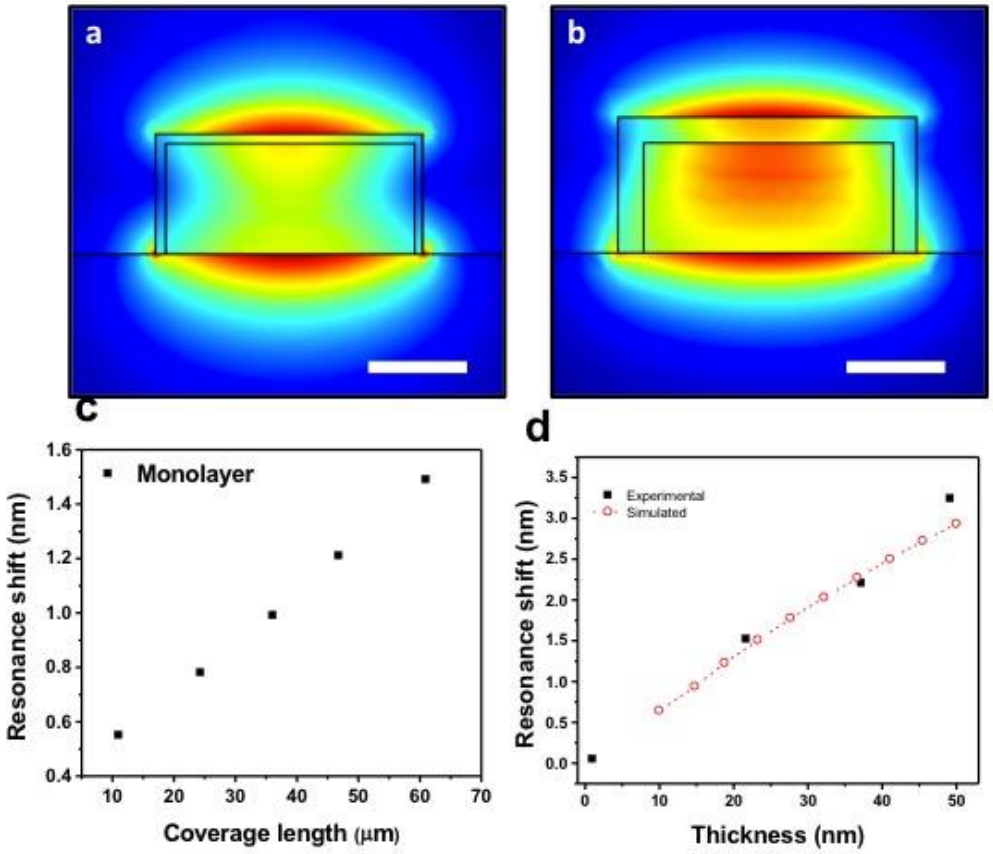

Figure 4 Mode profile (electric |E|-field) by Eigenmode analysis for the portion of the ring with MoS_2 transferred flakes (a) 20 nm and (b) 50 nm thick (Scale bar 200 nm). Variation of Resonance shift ($\Delta\boldsymbol{\lambda}$) and effective index change ($\Delta\boldsymbol{n_{eff}}$) extracted from (c) as a function of MoS_2 coverage length and (d) thickness, which is fully corroborated by a numerical simulation study.

The resonant wavelength (λ_{res}) of a MRR is proportional to the effective refractive index of the propagating mode in the circular waveguide (Tsigaridas, 2017). Therefore, the change in the effective mode index (Δn_{eff}) after transfer of the MoS_2 flakes, as compared to bare ring, is related to a change in resonance shift ($\Delta\lambda$) by following the eq. $\Delta n_{eff} = \frac{\Delta\lambda}{\lambda_{res}} * n_{eff,bare}$, where, $n_{eff,bare}$ is the effective mode index for bare waveguide. The effective index the for the bare waveguide can be found from FEM

Eigenmode analysis by choosing the T M-like mode in correspondence with our TM-grating designs used in measurements.

Since, here the MRR is partially covered by MoS_2 flakes the effective refractive index of the ring can be formulated as an effective length-fraction index via (Maiti et al., 2018),

$$n_{eff,ring} = \frac{(2\pi R - l) * n_{eff,bare} + l * n_{eff}}{2\pi R} \quad (3)$$

where R is the radius of the ring and l is the MoS_2 coverage length. The effective index for monolayer covered waveguide is found to be 1.723 for TM mode. The effective index (n_{eff}) for flakes with different thickness can be found using FEM Eigenmode analysis. The refractive index of the MoS_2 layer was taken from (Yim et al., 2014) and Si refractive index from (Pierce & Spicer, 1972). Figure 4(a) and (b) represent the normalized in-plane ($|E_x|$) electric field distribution for TM mode along with the device which integrates a layer of MoS_2 of 20 and 50 nm thickness, respectively. It is possible to observe that the higher intensity of the electric field within the MoS_2, layer and the consequently decreased leakages in air and substrate, suggest higher confinement for multi-layer MoS_2 (50 nm). Our measurement is designed for TM mode, which means that the electric field component parallel to the side walls (y-direction) is negligible. Thus, there is no significant interaction nor coupling between the evanescent wave and the flake leaning on the lateral side of the photonic waveguide. Hence, using Eq. (3), we can obtain Δn_{eff}, and hence the resonance shift ($\Delta\lambda$), which is shows an unequivocal correlation with our experimental data Figure 4(d). We map out the resonance shift ($\Delta\lambda$) as a function of MoS_2 flake thickness in Figure 4(d), (i) up to 50 nm and observe a resonance

shift per coverage length of 0.064 nm/μm, which is beyond the resolution limit of our spectrometer (~0.03 nm). The results indicate that mono-multilayer MoS_2 integrated on Si photonic platform could be an interesting choice for future active modulator devices at telecommunication wavelength.

2.4 Conclusion

The thesis successfully demonstrated the heterogeneous integration of MoS_2 with silicon photonic waveguides and micro-ring cavities and the interaction with it from monolayer to multi-layers. The variation in coverage length and thickness of the material will help to achieve the physical mechanism of tunable coupling due to change in coupling and loss coefficients. This study demonstrates a method to determine critical coverage for a given ring resonator which is an important parameter for obtaining a maximum extinction ratio for enabling active modulation. The resonance shift as a function of coverage and thickness of MoS_2 flakes was found to be 0.64 nm/μm correlating with the simulated results. The analysis and technique developed can be further used in characterizing and optimizing the heterogeneous integration of 2D materials on photonic and optoelectronic devices.

3. $MoTe_2$ integrated Photodetectors

3.1 Introduction

Among various optoelectronic devices, photodetectors are key components that convert optical signals into electrical signals (Ma et al., 2018). The performance of the photodetectors is based on the dark current levels and the photoresponsivity of the device for better photon detection. TMDCs as discussed before providing a strong light-matter interaction among 2D materials. $MoTe_2$ in the form of semiconducting 2H-phase has a layer dependent band gap extending up to the NIR (Ma et al., 2018). Therefore, $MoTe_2$ can be integrated with silicon photonics operating at telecommunication wavelength (1550 nm).

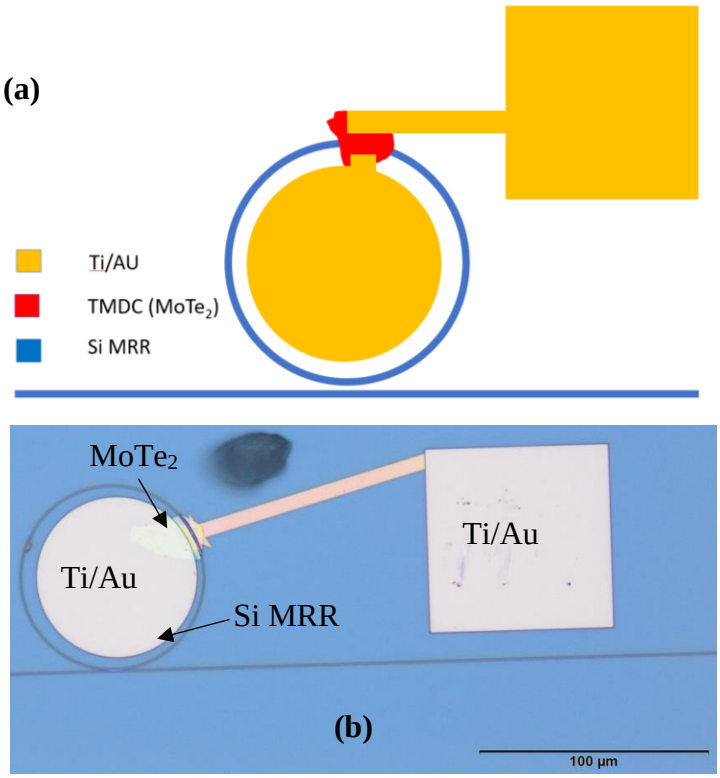

Figure 5 Few-layered $MoTe_2$ Photodetector on Si MRR (a) Conceptual schematic design of $MoTe_2$ photodetector fabricated on a Si MRR on SOI substrate (b) Optical microscopic image of the fabricated $MoTe_2$ photodetector. $MoTe_2$ flake was transferred on a Si MRR with two metal contacts of 45 nm gold on a 5 nm titanium layer (Ti/Au) forming the electrical contacts to the active material.

A laser light (1550 nm) signal was fiber coupled into the device via grating couplers and coupled into the device by silicon MRR.

In this thesis, a few-layer $MoTe_2$ waveguide photodetector operating at 1550 nm wavelength was designed and fabricated. The $MoTe_2$ few-layer flakes were transferred on SiP MRRs using physical exfoliation technique and 2D printer tool (Hemnani et al., 2018). The 2D material flake was connected in two terminal configurations. A nanoampere level dark current was measured with highly sensitive photodetection. The metal contacts were formed of Ti/Au:5 nm/45 nm. As Au has a work function ($\phi Au \approx 5.1$ eV) that aligns its Fermi level close to the valence band of the semiconducting MoTe2. The Schottky junction formed at the contacts significantly reduces the injection of carriers into MoTe2. Hence, giving rise to a very low dark current. The fabrication of such devices is less complicated and can be easily integrated with the measurement system. The basic design of the device and optical image of the actual device is as shown in Figure 5.

3.2 Methodology

The conceptual design of the photodetector and the fabricated $MoTe_2$ photodetector is presented in Figure 5 (a) and (b). The active material consists of a few-layer MoTe2 flake acting as the optically absorbing semiconducting material. The integration of TMDC ($MoTe_2$) was performed on taped out SiP chips (APPLIED NANOTOOLS INC.) to build the photodetectors, i.e. heterogeneous material integration into SiP. The samples are cleaned using acetone and then Isopropanol (IPA) and dried using nitrogen gas. The

sample was heated on a hot plate for 2-3 mins at 180^{o}C to remove humidity from the surface for better adhesion of the flakes (Uwanno, Hattori, Taniguchi, Watanabe, & Nagashio, 2015). The few layered $MoTe_2$ flakes were transferred on the micro-ring resonators (MRR) using our in-house developed 2D printer tool (Hemnani et al., 2018). In brief, the $MoTe_2$ flakes were exfoliated by using scotch tape and transferred on a thin PDMS substrate. The 2D printer was used to transfer the flakes from PDMS accurately on the desired part of the device i.e. the ring in this case. The MoTe2 flake is well aligned to the silicon MRR beneath it so that the guided light can efficiently be absorbed via an evanescent coupling. After the transfer process, a thin layer of PMMA (~300 nm) was spin coated on the sample at 1500 rpm and was post-baked at 180^{o}C for two minutes. The position of the flake is then imaged using a microscope mounted with a high-resolution camera. This image is useful for finding the exact position of the flake on the device by using the image-mapping technique. The captured image is converted to 24-bit Bitmap format. This converted image is then loaded in the CAD file of the device design. The image is then scaled to the size of the device. The probes are designed based on the size and shape of the flake on each device as shown in Figure 5. The size of the contact pads is designed as 80 microns * 80 microns and the inner contact pad is 35 microns in radius (radius of the ring is 40 microns). The complete image mapping steps can be seen in Figure 6. This design is then patterned using electron beam lithography process. The sample is then developed in MIBK:IPA::3:1 solution for development. A thin layer of 5 nm titanium followed by 45 nm gold is deposited using electron beam evaporation process. The lift-off process is performed by using acetone. The distance between the

contacts on the flake was in a few microns range that can be seen from the SEM image of the device in Figure 8 (b).

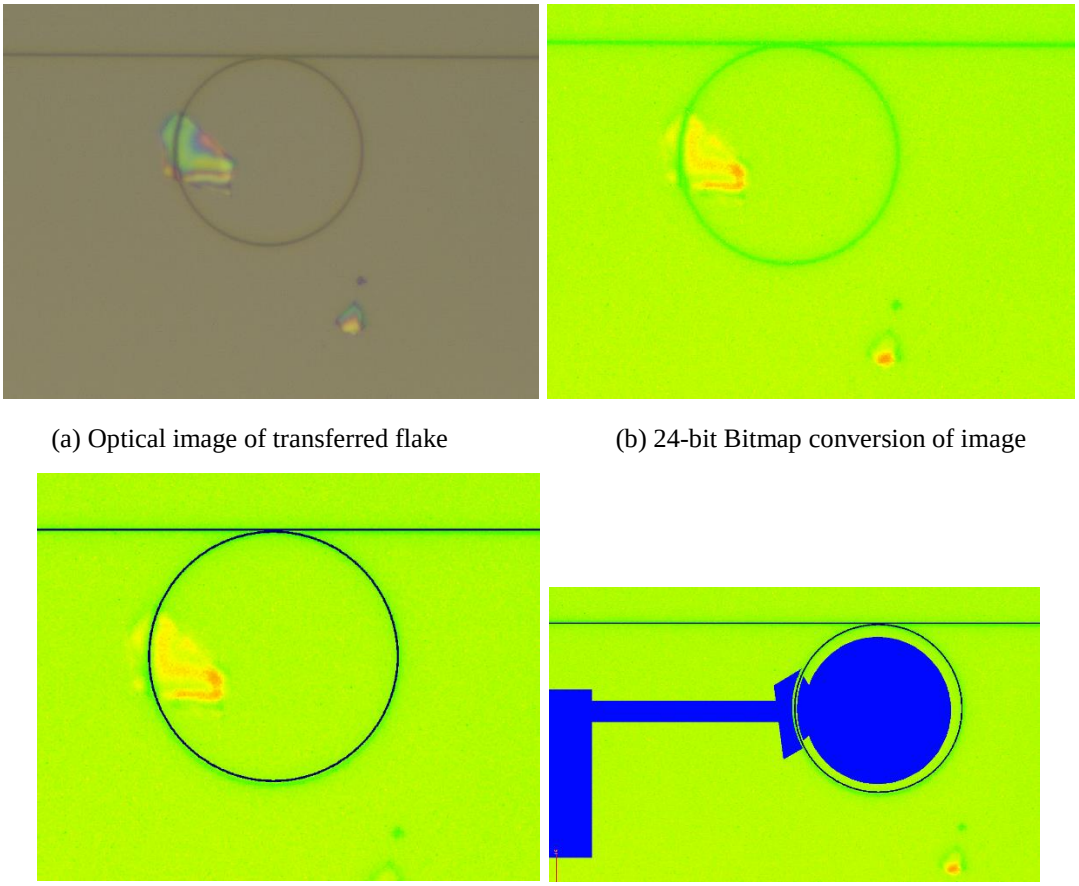

(a) Optical image of transferred flake

(b) 24-bit Bitmap conversion of image

(c) Scaled bitmap image over the position of design in CAD file flake

(d) Design of contacts based on of the design

Figure 6 Position mapping of MoTe2 flake for contact pad designing (a) Optical image captured at 20x magnification after PMMA (~300nm) layer was coated (b) The image was converted to 24-bit Bitmap format using Microsoft Paint software maintaining the size of image (c) The image was scaled to the device size in the CAD file to determine the exact position of the $MoTe_2$ flake (d) The contact pads and probes were designed based on the size and shape of the flake observed from the image

It is experimentally reported by (Gao et al., 2016) that thin layers of TMDCs exhibit poor long-term stability in air. After room-temperature exposure to the environment for a prolonged period, the

TMDCs undergo aging effects like extensive cracking and changes in morphology. This adversely degrades the material and deteriorates the device performance. The reason behind this degradation is the gradual oxidation along the grain boundaries and the adsorption of organic contaminants from the surroundings (Gao et al., 2016). Therefore, the final step is completed by coating the sample chip with PMMA (~300 nm) following the same procedure as explained at the beginning. The

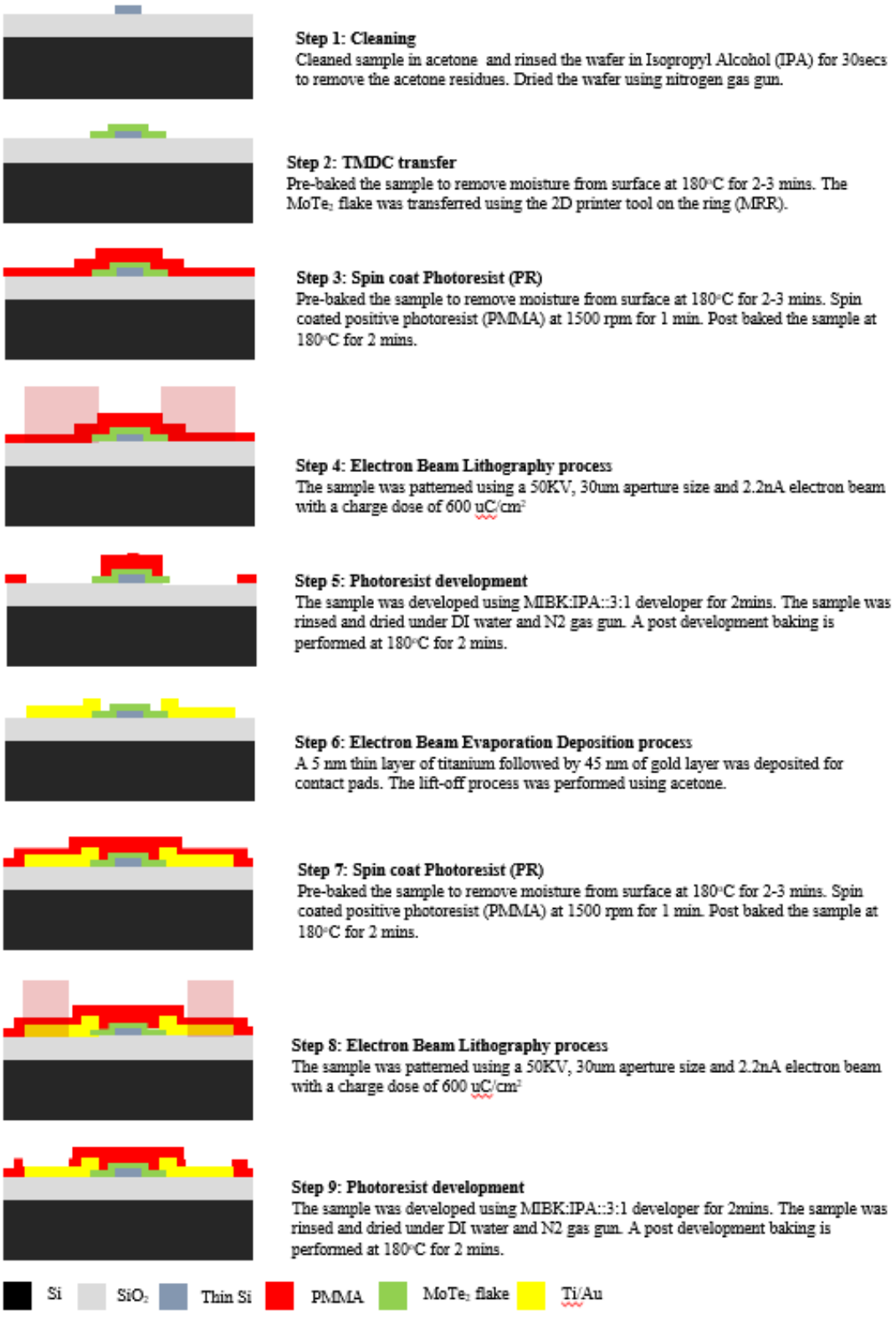

Figure 7 Fabrication of photodetector using MoTe2 as the active material. The pre-baking process at Step 2 is very important to remove humidity as it reduces the adhesion of the flake with the substrate and the device. The humidity forms small bubbles under the flake during the rest of the steps due to

high temperatures involved in the processes affecting the contact with the Si MRR. The spin speed while coating PMMA in Step 3 and Step 7 was reduced from 4000rpm to 1500 rpm to avoid the flakes from moving away from the transferred position due to the viscosity of the PMMA.

PMMA layer acts as both a passivation layer for TMDC to protect from oxidation and as a cladding for the SiP devices enhancing the coupling efficiency of the grating couplers. This strategy is implemented to prevent the degradation of the thin TMDC material from accelerated aging due to high-temperature and oxygen-rich environment conditions. An electron beam lithography (EBL) process is performed at end to open the electrical contact pads for probing by patterning a window as shown in Figure 7.

A transverse magnetic-polarized (TM) tunable laser at a wavelength of 1550 nm was used as the light source and coupled into and out of the device from the input and output grating couplers of the Si MRR. A DC power supply was used to bias the device and a power meter was used to determine the current flowing through the device. The measurement setup consisted of a fiber coupled optical measurement system to couple light using an optical fiber via input grating coupler and sense using another optical fiber from the output grating coupler. A pair of standard electrical probes were used on the setup to electrically bias the device and measure the photocurrent.

3.3 Results and Discussion

The static performance characteristics of the $MoTe_2$ photodetector were performed by measuring the photocurrent of the device as a function of the incident light power at a bias voltage range from −4 V to 4V. A photoresponsivity of 0.5 A/W is obtained which is comparable to one-sided graphene/Au contacted $MoTe_2$ photodetector (Ma et al., 2018).

The photoexcited electrons and holes are collected under both forward and reverse biases efficiently as the few layers $MoTe_2$ flake

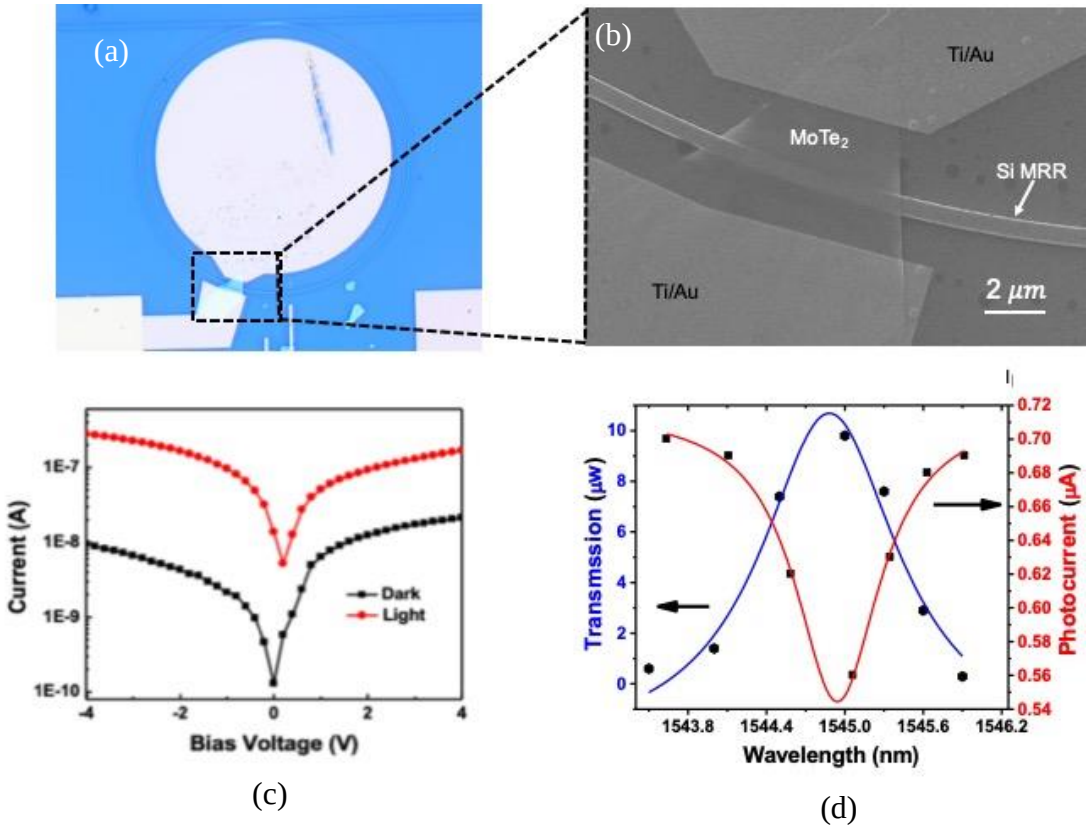

Figure 8 $MoTe_2$ photodetector analysis (a) Optical microscopic image of the fabricated $MoTe_2$ photodetector (b) Magnified SEM image of the device showing the $MoTe_2$ flake with two metal contacts above the Si MRR (c) Logarithm-scale I−V curves without light (black line) and with light (red line) (d) Measured output transmission power (blue line) from the output grating coupler of Si MRR and photocurrent (red line) from the two terminals of the device with respect to wavelength showing the maximum peaks.

absorbs the incident photons via indirect band-to-band transitions. Current-voltage (I−V) curves were measured both in the dark and upon light incidence on the device as shown in Figure 8 (c). It was observed that the magnitude of the photocurrent increases with an increase in optical power. The number of photons absorbed increases leading to an increase in photogenerated carriers being collected. As shown in Figure 3b, the photoresponsivity increases with the bias voltage, as more carriers can be extracted

before recombination. The wavelength-dependent photocurrent and transmission output are plotted in Figure 8 (d), by using a tunable laser operating at 1550 nm. The absorption of a MoTe2 flake depends on both the layer thickness and length of the flake (Keum et al., 2015; Ruppert, Aslan, & Heinz, 2014). The contact pads are placed away from the waveguide to avoid extrinsic losses and reduction of quantum efficiency. The thickness of the flake cannot be controlled during the transfer process as it is difficult to measure the thickness of the flake on a transparent substrate (PDMS). Also, the length of the flake cannot be precisely controlled in the exfoliation process due to randomness in the peeling of the layers.

3.4 Conclusion

The use of TMDC materials demonstration for the active tunable device (here photodetectors) was performed successfully. The design and fabrication of the few layered $MoTe_2$ based photodetectors were engineered using various imaging and fabrication techniques. The distance between the contact pads was engineered such that the extrinsic optical loss in Si MRR is not induced. The photoresponsivity of the device was measured experimentally to be 0.5 A/W with the very less dark current of 5 nA at the operating wavelength of 1550 nm. This device design can be further enhanced by changing the coverage length and thickness of the flake for optimal results as there exists a trade-off between photoresponsivity and dark current of the photodetectors leading to limit of the speed of the device based on variation in thickness and size (Ma et al., 2018).

4. Silicon Nitride-based Platform for Photonic Devices

4.1 Introduction

The thesis advances further with the investigation of the effect of the TMDCs on the photonic devices in the visible spectrum (here at 640 nm). The traditional Si photonics has shown phenomenal progress in the field of telecommunication for 1550 nm and 1310 nm wavelengths. But, silicon cannot be used for building devices for optical processes at 640 nm due to its bandgap (1.1eV) where the visible spectrum is absorbed, and the material is opaque. SiP is built on a silicon-on-insulator (SOI) substrate. It provides a high index contrast for the waveguides and devices. Silicon nitride photonics comparatively provides a moderate index contrast. Another significant property of using silicon nitride is that it is CMOS compatible and can be integrated with SOI platform as well for a few applications. The optical loss in silicon nitride is almost zero or negligible due to higher bandgap as compared to silicon. The two-photon absorption is absent in silicon nitride due to its large bandgap whereas it increases with the optical power in silicon. The third order nonlinearity effects like the Kerr effect is weak in silicon nitride and very strong in silicon due to the two-photon absorption (Baets et al., 2016/03/20). The property differences are summarized in Table 2. This chapter of the thesis deals with the design and fabrication of waveguides and grating couplers for development of photonics platform operable at 640 nm wavelength.

Being an emerging technology, development and fabrication of silicon nitride photonics platform are performed by very few fabrication industries. Major foundries are involved in the SiP platform fabrication and development and are reluctant to shift to a new fabrication process. This leaves the commercialization of the silicon nitride platform

as a monopoly for the few industries involved in it. Also, the optimization of this platform for different photonic devices is still in progress among researchers. As a trending technological advancement, the cost of silicon nitride platform is very high and yet delivered with moderate performances. The thesis, therefore, focuses on the development of silicon nitride photonics platform for optoelectronic applications in the visible spectrum.

The fabrication process of the silicon nitride photonic waveguides and grating couplers is crucial for building any other devices as micro-ring resonators, Mach-Zehnder interferometers and more of such devices. The gratings are used to couple the light from a free space Gaussian laser beam into the devices on the chip. The waveguides facilitate the routing of coupled light to different devices for further

Properties	**SOI**	**SIN**
Refractive Index contrast (Silica Cladding)	High (3.5/1.5)	Low (2/1.5)
Transparency range	1.1 um – 3.7 um	Visible – 500nm
Waveguide Loss	1-2 dB/cm	0.001 – 0.002 dB/cm (x1000 better)
Two-photon absorption	Loss increase with power	Virtually zero due to the large band gap
Kerr effect	Strong	Weak

Table 2 Silicon versus Silicon Nitride properties for optical applications (Baets et al., 2016/03/20)

processing of the information. The grating couplers are characterized based on their coupling efficiency, which is defined as the ratio of input optical power to the output optical power. The other aspects of designing a grating coupler are periodicity, duty

cycle, and depth (height). A resonant coupling between the guided light in the silicon nitride layer and a diffraction order of the grating is given by:

$$\beta = \sin(\theta_{inc})\, k_0 n_{nic} + p\frac{2\pi}{\Lambda}$$

where $k_0 = 2\pi/\lambda$, λ is the wavelength, n_{inc} is the refractive index of the top cladding layer (here air), θinc is the incidence angle (here ~ 90 degrees), p is the diffraction order (here p = +1), Λ is the grating period, $\beta = k_0$neff is the real part of the propagation constant, and neff is the effective index of the guided light in the tapered waveguide.

The fabrication of the grating couplers and waveguides was carried out using a wafer with a thin layer of LPCVD grown silicon nitride (~220 nm) on a thick layer of silicon oxide (2 microns) on a silicon substrate.

4.2 Methodology

The wafer was cut into small square pieces of 1 cm *1 cm for small chip sizes. The sample was cleaned using acetone and then Isopropanol (IPA) and dried using nitrogen gas. The sample was heated on a hot plate for 2-3 mins at 180^{o}C to remove humidity from the surface for better adhesion of the flakes. The samples were spin coated with a negative photoresist (ARN 7520.18) at 4000 rpm for one minute. The sample was post-baked at 85^{o}C for 90 seconds. The design for grating and waveguides coupler as shown in Figure 9 was patterned using electron beam lithography process. The acceleration voltage of the beam was 50kV, aperture size was 20 microns and the current was 63 pA. The sample was then developed using MF319 developer for 90 seconds. It was observed that the structures of the device were damaged while the development process and rinsing the sample as shown in Figure 11. The development process was carried out without any

mechanical vibrations induced in the beaker to avoid damage to the very small features like grating couplers. The sample was then plasma etched using CHF3 gas with 12sccm with O_2 gas with 2 sccm concentration. The power of the plasma was set to 200W and the etch time was 8 minutes. This etch recipe was optimized after multiple runs been performed in hand to calibrate the etch depth and etch speed for better control over-etching process.

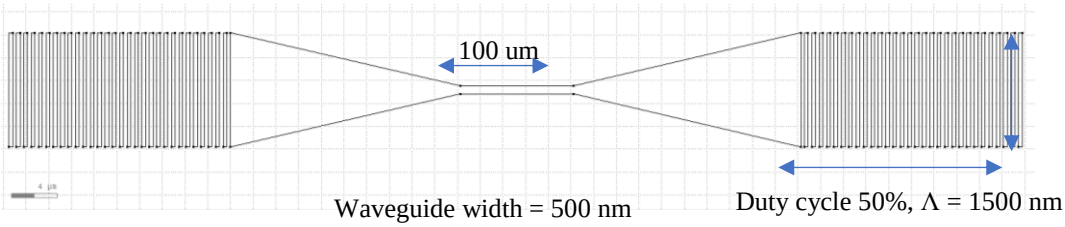

Figure 9 Design of waveguide and grating coupler: The duty cycle of the grating couplers was 50% and the period was 1500 nm. The width of the waveguide is 500nm and the length is 100 um. The depth of the grating coupler is ~215 nm.

After the etch process the sample was rinsed thoroughly in acetone to get rid of the negative photoresist. The issues like lateral etch, undercuts and over-etching were optimized by changing the dose values of the electron beam during lithography and changing the concentration of the etchants. The complete fabrication process steps and parameters can be referred from Figure 10.

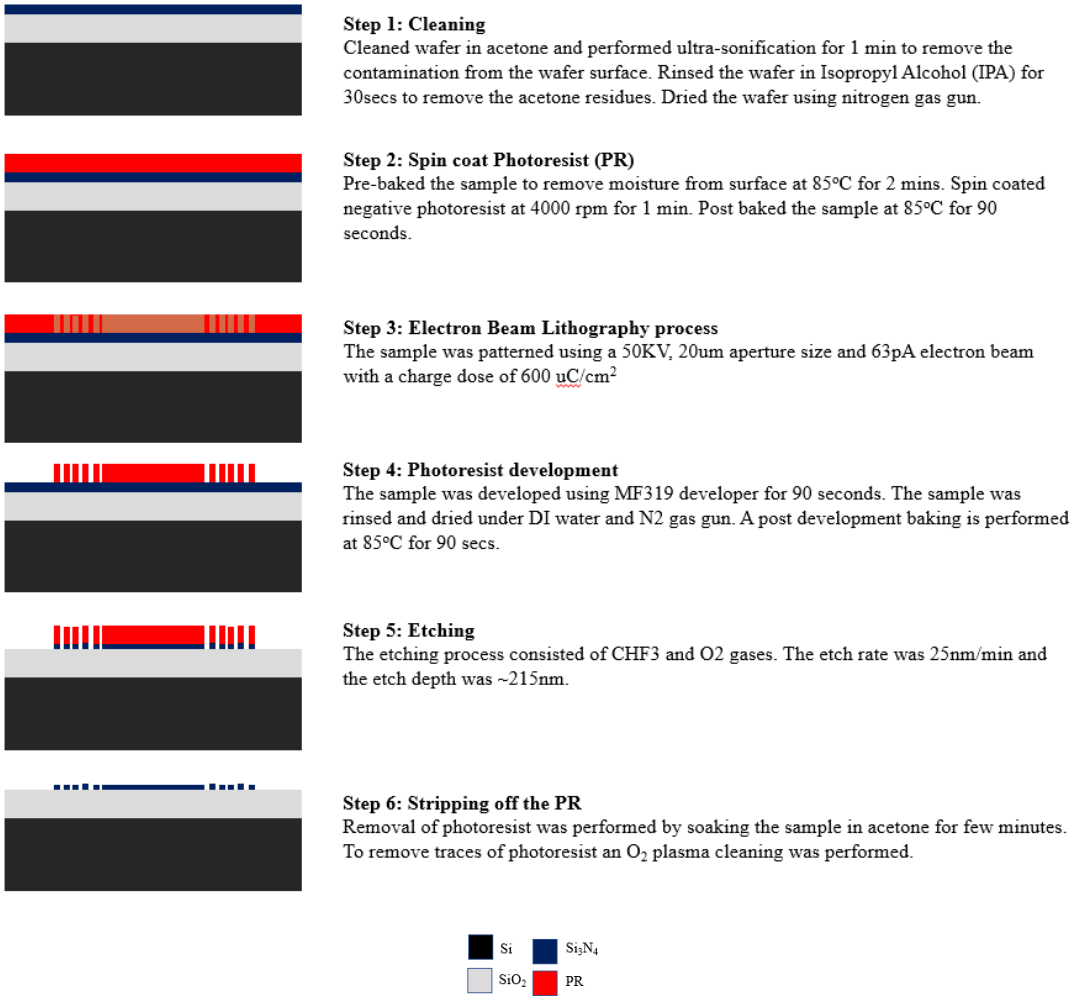

Figure 10 Silicon Nitride waveguides and grating couplers fabrication process The current and dose values were optimized for over-dose and under-dose effects on the negative photoresist. The electron beam lithography speed was reduced for patterning the grating couplers for better resolution and control over exposure time. A lateral etch of 10-15 nm was observed in Step 5 reducing the effective size of the waveguide to ~470-480 nm and period of ~1520-1530 nm. The duty cycle was shifted to ~53%. The devices working even with these variations but with lower efficiency due to loss caused majorly by reflection and scattering.

The dose values for the electron beam during the lithography process were increasingly varied by 10 uC/cm^2 with the starting dose value as 500 uC/cm^2. After optimization, the dose value in the range of 750 uC/cm^2 – 800 uC/cm^2 was found to be ideal for the features designed. The samples were always observed under Secondary Electron Microscope (SEM) to verify the edge and surface roughness of the device. SEM also

helps in determining the undercuts due to etching by placing the sample vertically on edge for observation as shown in Figure 13.

After the fabrication, the devices were tested using a free space setup. A tunable laser

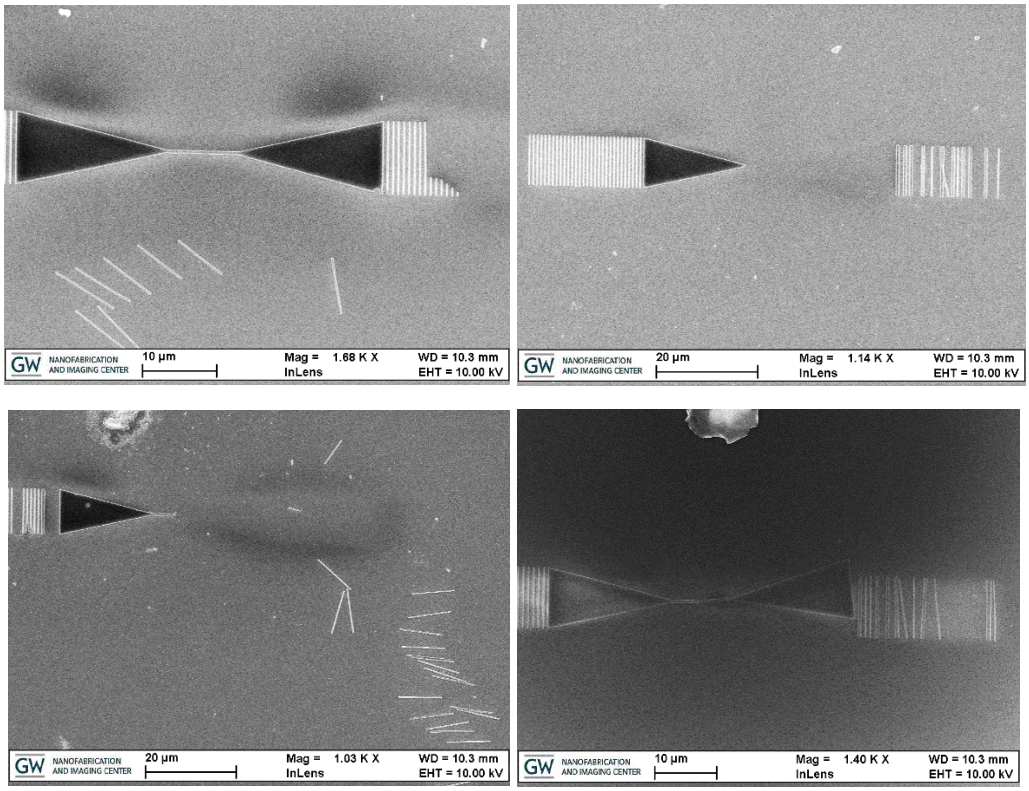

Figure 11 SEM images of damage to structures during development and rinsing of the sample during fabrication

with operating range in the visible and near-infrared spectrum. The devices were tested initially for wavelengths between 500 nm to 680 nm. The Gaussian laser beam is aligned with the input grating coupler vertically at ~90 degrees. The output was captured using a CMOS camera mounted on the microscopic lens. The image was processed using a MATLAB script by identifying the input and output regions of the device and integrating the intensity values in those regions.

4.3 Results and discussion

After multiple samples were fabricated, tested and rigorous optimizations in the fabrication process and design were made, a few devices worked successfully. The period of the grating coupler was 1500 nm and the duty cycle was 53% with a etch depth (height of the device) of 215 nm. The efficiency of the grating couplers was computed

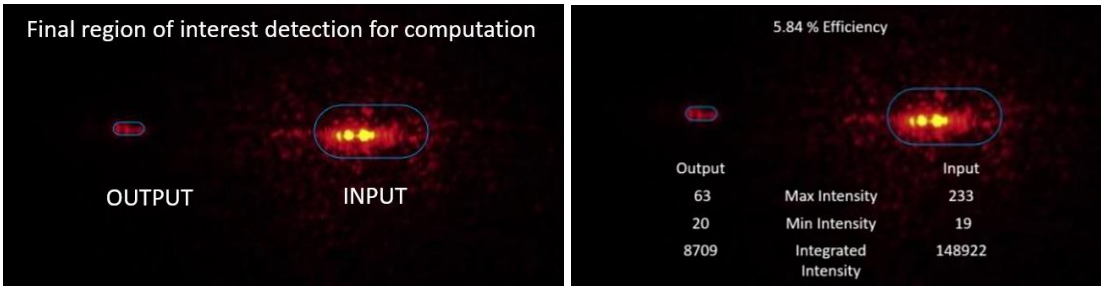

Figure 12 Image processing using MATLAB for the integration of intensities

by using the MATLAB script by integrating the intensity values as shown in Figure 12. The grating coupler efficiency of approximately 5.84 % was achieved for a laser beam at 640 nm wavelength. Figure 13 shows the SEM image of the grating couplers in vertical edge orientation.

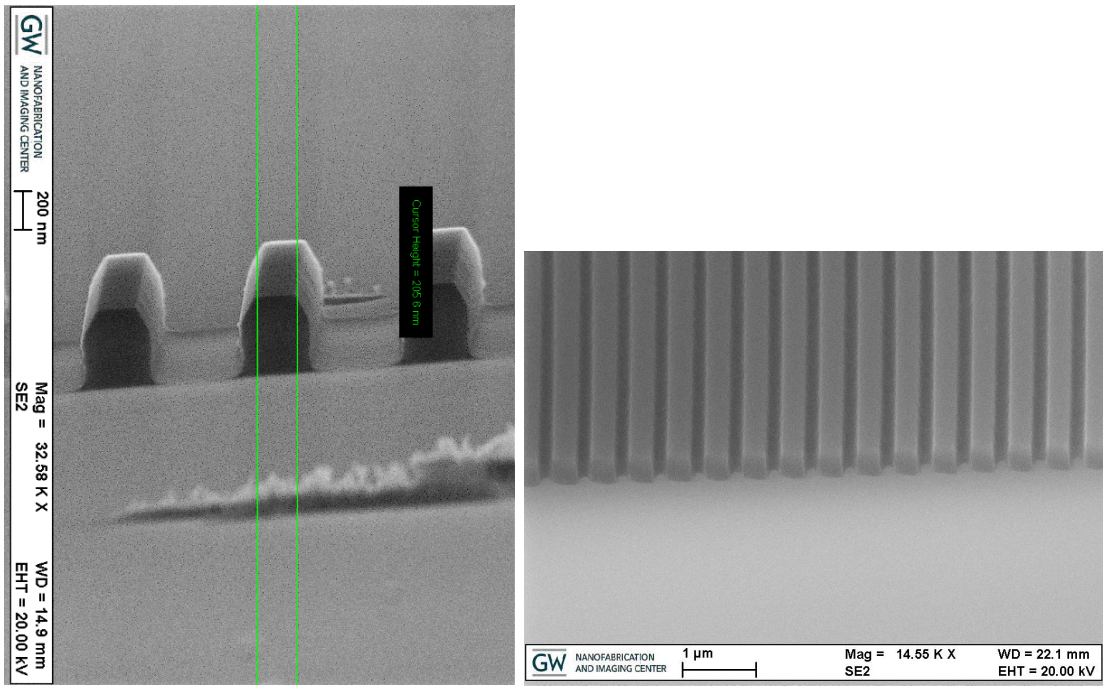

(a) (b)

Figure 13 SEM of Grating Coupler (a)Vertical edge of Grating coupler. The sample was placed at ~90 degrees on the sample holder of the SEM machine. The moving stage of the SEM was titled by an angle of 1.68 degrees to capture the side view of the grating coupler (b)Top view of the grating coupler with a tilt of 30 degrees to observe the smoothness of the walls by using SEM.

The sample was placed on the holder at 90 degrees, and the stage was tilted at 1.68 degrees, to obtain this image for a side view of the grating coupler. The edge roughness was minimized and can be observed in Figure 14.

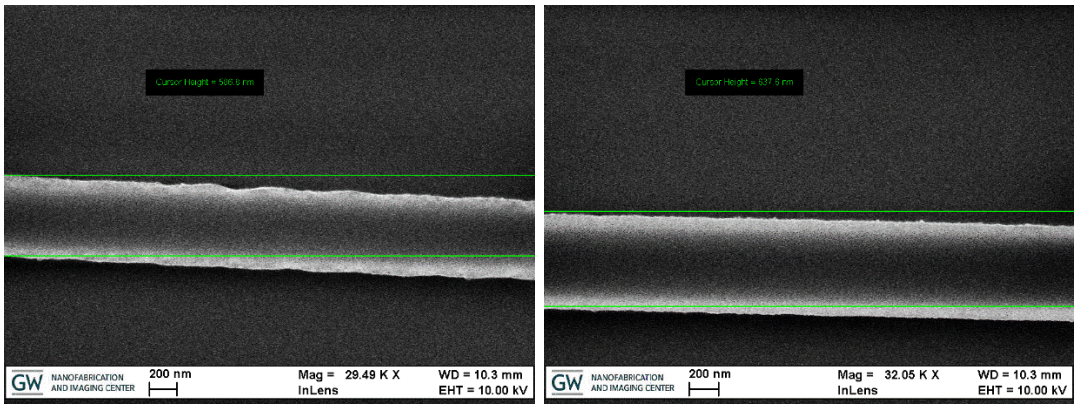

(a) (b)

Figure 14 Edge roughness improvement (a) Before optimizations the sidewall roughness was ~5 nm - 6 nm (b) After Optimizations the sidewall roughness was < ~4 nm. The roughness was calculated using a MATLAB program but for accurate measurements a Focused Ion Beam (FIB) SEM is required.

4.4 Conclusion

The design and fabrication of waveguides and grating couplers were successfully presented. The various optimizations in the fabrication process were performed and change in results was observed. The linear type of grating coupler was chosen over focused beam grating couplers as the measurement system used was free space system as the latter is used for fiber coupled measurement system. The grating coupling efficiency of 5.84% was achieved from the measuring devices. The devices were designed to operate in 640 nm wavelength. The coupling efficiency is very low as compared to the other literature work (Romero-García, Merget, Zhong, Finkelstein, & Witzens, 2013; Subramanian et al., 2012). The prime reason for such a low efficiency is the lateral etch caused in etching leading to change in the period and duty cycle of the grating couplers. This in effect shifts the critical coupling of the wavelength of the grating coupler leading to scattering and reflection of the input light. This platform can be further optimized to increase the coupling efficiency of the grating couplers and develop more devices like micro-ring resonators, Mach-Zehnder interferometers, and other photonic devices. An addition of the pedestal layer between the grating couplers has been reported by (Hosseini, Yegnanarayanan, Atabaki, Soltani, & Adibi, 2009) to enhance the coupling of light. A thin layer of silicon nitride is left unetched at the foot of the grating coupler by precisely controlling the etch rate. This layer helps in increasing the coupling efficiency of the grating coupler as the in-plane coupling increases. The development of the silicon

nitride platform for photonic devices can be improved with rigorous optimizations in process steps and engineering the device dimensions.

5. Challenges

Inventions made in its crude form have always been challenging in terms of ease of use and reliability. The time and efforts play an important role in development, optimization, and changes to be embedded in those inventions. Like the first version of computers using the vacuum tubes and almost of the size of a room was not possible to be understood by common people. In the matter of time and efforts being made to improve these systems we now have computers in micron scale with high computational capabilities. Similarly, this thesis research has also been through challenges in terms of using tools, services, and resources for completing this study.

The use of a 2D printer developed by (Hemnani et al., 2018) was a key tool which helped in the integration of the 2D materials with devices. But, as mentioned before it was difficult initially to operate the tool due to lack of information and difficulties with the setup. The stamping technique and stability of the setup were prime concerns while transferring the flakes. The stamper due to instability sometimes led to damage to the device and consumed plenty amount of time for transfer of flakes on the devices due to alignment issues. Eventually, these problems were solved step by step and a summary is appended in the Appendix of this report.

The fabrication of all the devices was carried out in the Nanofabrication facilities of the George Washington University (GW-Fab) and the cleanroom facilities in National Institute of Standards and Technology (NIST) lab. The major part of the work was completed in GW-Fab. The process tools for electron beam lithography, etching, deposition, Secondary electron microscopy, atomic layer deposition, profilometers, and wet chemistry benches were used in this project. All the set of equipment is one of kinds

kind and made the fabrication of devices smooth and easy. But, due to the improper maintenance schedule and lack of calibration often the machines were not available for use. The samples were then processed in NIST labs which slowed down the work for days to week due to transport and availability of tools in NIST. This certainly delayed a lot of work in this research ultimately leading to a loss in publishing the work and failed in claiming the research findings being the first. The delay led to papers being published with similar work by other research groups before us with similar results we estimated and found later.

Besides the unavailability of facilities, a lot of time was wasted waiting for ordering the required materials for research as it took weeks and months to process the purchase request by the financial department of the university. This can be improved by the higher authorities so that the materials required for the research purposes can be ordered immediately. This certainly has been affecting the pace of research as without the correct tools and resources the project cannot proceed in any direction.

Every step in this journey was a lesson to be learned and has enlightened the thought of research approach and troubleshooting the techniques, methods and plans developed. It was an amazing and fruitful experience in dealing with multiple types of situations and problems to achieve one single goal.

6. Conclusion

This thesis reported the results of research that studied the effects of TMDCs on photonic devices to develop passive devices by analyzing and measuring the change in loss and effective refractive index of the SiP devices. A relation between these effects, and the coverage length and thickness of the TMDC flakes, was obtained. Further, the design and fabrication of an actively tunable photodetector were performed. A dark current 5 nA and photoresponsivity of 0.5 A/W were achieved from the fabricated device.

Finally, the thesis research also dealt with the fabrication of silicon nitride photonic platform for operation in the visible frequency domain. The waveguides and grating couplers functional at the 640 nm wavelength were successfully tested. A 5.84 % efficient grating couplers was designed, fabricated and tested using a free space measurement system.

This thesis research can be further advanced by designing and fabricating active tunable devices like photodetectors and modulators in the visible spectrum by using the silicon nitride photonic platform. The characterization of more TMDC materials can be studied for exploring and widening the scope of integration of these materials for various optoelectronic applications.

References

2D material printer. . ().[Video/DVD] Retrieved from https://sorger.seas.gwu.edu/2d-material-printer.html

2D materials. (2016). Retrieved from https://www.nature.com/collections/kdhntrhbps

Amin, R., Ma, Z., Maiti, R., Khan, S., Khurgin, J. B., Dalir, H., & Sorger, V. J. (2018). Attojoule-efficient graphene optical modulators. *Applied Optics*, *57*(18), D140. doi:10.1364/AO.57.00D130

Baets, R., Baets, R., Subramanian, A. Z., Subramanian, A. Z., Clemmen, S., Clemmen, S., . . . Severi, S. (2016/03/20). (2016/03/20). Silicon photonics: Silicon nitride versus silicon-on-insulator. Paper presented at the Th3J.1. doi:10.1364/OFC.2016.Th3J.1 Retrieved from https://www.osapublishing.org/abstract.cfm?uri=OFC-2016-Th3J.1

Bie, Y., Grosso, G., Heuck, M., Furchi, M. M., Cao, Y., Zheng, J., . . . Jarillo-Herrero, P. (2017). A $MoTe_2$-based light-emitting diode and photodetector for silicon photonic integrated circuits. *Nature Nanotechnology*, *12*(12), 1124-1129. doi:10.1038/nnano.2017.209

Cao, D. H., Stoumpos, C. C., Farha, O. K., Hupp, J. T., & Kanatzidis, M. G. (2015). 2D homologous perovskites as light-absorbing materials for solar cell applications. *Journal of the American Chemical Society*, *137*(24), 7843-7850. doi:10.1021/jacs.5b03796

Datta, I., Chae, S. H., Bhatt, G. R., Li, B., Yu, Y., Cao, L., . . . Lipson, M. (2018/05/13). (2018/05/13). Giant electro-refractive modulation of monolayer WS2 embedded in photonic structures. Paper presented at the STu4N.7. doi:10.1364/CLEO_SI.2018.STu4N.7 Retrieved from https://www.osapublishing.org/abstract.cfm?uri=CLEO_SI-2018-STu4N.7

Ding, Y., Zhu, X., Xiao, S., Hu, H., Frandsen, L. H., Mortensen, N. A., & Yvind, K. (2015). Effective electro-optical modulation with high extinction ratio by a Graphene–Silicon microring resonator. *Nano Letters, 15*(7), 4393-4400. doi:10.1021/acs.nanolett.5b00630

Freitag, M. (2008). Graphene: Nanoelectronics goes flat out. *Nature Nanotechnology, 3*(8), 455-457. doi:10.1038/nnano.2008.219

Gang Hee Han, Nicholas J Kybert, Carl H Naylor, Bum Su Lee, Jinglei Ping, Joo Hee Park, . . . A T Charlie Johnson. (2015). Seeded growth of highly crystalline molybdenum disulphide monolayers at controlled locations. *Nature Communications, 6*(1), 6128. doi:10.1038/ncomms7128

Gao, J., Li, B., Tan, J., Chow, P., Lu, T., & Koratkar, N. (2016). Aging of transition metal dichalcogenide monolayers. *ACS Nano, 10*(2), 2628-2635. doi:10.1021/acsnano.5b07677

Geim, A. K., & Novoselov, K. S. (2007). The rise of graphene. *Nature Materials, 6*(3), 183-191. doi:10.1038/nmat1849

Hemnani, R. A., Tischler, J. P., Carfano, C., Maiti, R., Tahersima, M. H., Bartels, L., . . . Sorger, V. J. (2018). 2D material printer: A deterministic cross contamination-free transfer method for atomically layered materials. *2D Materials, 6*(1), 015006. doi:10.1088/2053-1583/aae62a

Keum, D. H., Cho, S., Kim, J. H., Choe, D., Sung, H., Kan, M., . . . Lee, Y. H. (2015). Bandgap opening in few-layered monoclinic $MoTe_2$. *Nature Physics, 11*(6), 482-486. doi:10.1038/nphys3314

Kim, D., Sun, D., Lu, W., Cheng, Z., Zhu, Y., Le, D., . . . Bartels, L. (2011). Toward the growth of an aligned single-layer MoS2 film. *Langmuir, 27*(18), 11650-11653. doi:10.1021/la201878f

Kis, A., Giacometti, V., Brivio, J., Radenovic, A., & Radisavljevic, B. (2011). Single-layer MoS 2 transistors. *Nature Nanotechnology*, *6*(3), 147-150. doi:10.1038/nnano.2010.279

Lee, B., Liu, W., Naylor, C. H., Park, J., Malek, S. C., Berger, J. S., . . . Agarwal, R. (2017). Electrical tuning of Exciton–Plasmon polariton coupling in monolayer MoS2 integrated with plasmonic nanoantenna lattice. *Nano Letters, 17*(7), 4541-4547. doi:10.1021/acs.nanolett.7b02245

Lienau, C., Noginov, M. A., & Lončar, M. (2014). Light–matter interactions at the nanoscale. *Journal of Optics, 16*(11), 110201. doi:10.1088/2040-8978/16/11/110201

Ma, P., Flöry, N., Salamin, Y., Baeuerle, B., Emboras, A., Josten, A., . . . Leuthold, J. (2018). Fast MoTe2 waveguide photodetector with high sensitivity at telecommunication wavelengths. *ACS Photonics*, *5*(5), 1846-1852. doi:10.1021/acsphotonics.8b00068

Maiti, R., Hemnani, R., Amin, R., Ma, Z., Tahersima, M., Empante, T. A., . . . Sorger, V. J. (2018). *Microring resonators coupling tunability by heterogeneous 2D material integration* Retrieved from https://www.openaire.eu/search/publication?articleId=od_____18::6a744beee727bfc7b70b7afaaebabe1e

Maiti, R., Patil, C., Hemnani, R. A., Miscuglio, M., Amin, R., Ma, Z., . . . Sorger, V. J. (2019). Loss and coupling tuning via heterogeneous integration of MoS2 layers in silicon photonics [invited]. *Optical Materials Express*, *9*(2), 751. doi:10.1364/OME.9.000751

Mak, K. F., Lee, C., Hone, J., Shan, J., & Heinz, T. F. (2010). Atomically thin ${\mathrm{MoS}}_{2}$: A new direct-gap semiconductor. *Physical Review Letters*, *105*(13), 136805. doi:10.1103/PhysRevLett.105.136805

Manzeli, S., Ovchinnikov, D., Pasquier, D., Yazyev, O. V., & Kis, A. (2017). 2D transition metal dichalcogenides. *Nature Reviews Materials*, *2*(8), 17033. doi:10.1038/natrevmats.2017.33

Miller, D. A. B. (2017). Attojoule optoelectronics for low-energy information processing and communications. *Journal of Lightwave Technology, 35*(3), 346-396. doi:10.1109/JLT.2017.2647779

Morozov, S. V., Novoselov, K. S., Katsnelson, M. I., Schedin, F., Elias, D. C., Jaszczak, J. A., & Geim, A. K. (2008). Giant intrinsic carrier mobilities in graphene and its bilayer. *Physical Review Letters, 100*(1), 016602. doi:10.1103/PhysRevLett.100.016602

Phare, C. T., Daniel Lee, Y., Cardenas, J., & Lipson, M. (2015). Graphene electro-optic modulator with 30 GHz bandwidth. *Nature Photonics, 9*(8), 511-514. doi:10.1038/nphoton.2015.122

Pierce, D. T., & Spicer, W. E. (1972). Electronic structure of amorphous si from photoemission and optical studies. *Physical Review B, 5*(8), 3017-3029. doi:10.1103/PhysRevB.5.3017

Ruppert, C., Aslan, O. B., & Heinz, T. F. (2014). Optical properties and band gap of single- and few-layer MoTe2 crystals. *Nano Letters, 14*(11), 6231-6236. doi:10.1021/nl502557g

Splendiani, A., Sun, L., Zhang, Y., Li, T., Kim, J., Chim, C., . . . Wang, F. (2010). Emerging photoluminescence in monolayer MoS2. *Nano Letters, 10*(4), 1271-1275. doi:10.1021/nl903868w

Sun, Z., Martinez, A., & Wang, F. (2016). Optical modulators with 2D layered materials. *Nature Photonics, 10*(4), 227-238. doi:10.1038/nphoton.2016.15

Tsigaridas, G. N. (2017). A study on refractive index sensors based on optical micro-ring resonators. *Photonic Sensors, 7*(3), 217-225. doi:10.1007/s13320-017-0418-0

Ugeda, M. M., Bradley, A. J., Shi, S., da Jornada, F. H., Zhang, Y., Qiu, D. Y., . . . Crommie, M. F. (2014). Giant bandgap renormalization and excitonic effects in a monolayer transition metal dichalcogenide semiconductor. *Nature Materials, 13*(12), 1091-1095. doi:10.1038/nmat4061

Uwanno, T., Hattori, Y., Taniguchi, T., Watanabe, K., & Nagashio, K. (2015). Fully dry PMMA transfer of graphene on h-BN using a heating/cooling system. *2D Materials, 2*(4), 041002. doi:10.1088/2053-1583/2/4/041002

White, I. M., & Fan, X. (2008). On the performance quantification of resonant refractive index sensors. *Optics Express, 16*(2), 1020. doi:10.1364/OE.16.001020

Xiao, Y., Liu, Y., Li, B., Chen, Y., Li, Y., & Gong, Q. (2012). Strongly enhanced light-matter interaction in a hybrid photonic-plasmonic resonator. *Physical Review A, 85*(3), 031805. doi:10.1103/PhysRevA.85.031805

Ye, Y., Wong, Z. J., Lu, X., Ni, X., Zhu, H., Chen, X., . . . Zhang, X. (2015). Monolayer excitonic laser. *Nature Photonics, 9*(11), 733-737. doi:10.1038/nphoton.2015.197

Yeh, C. (2012). *Applied photonics* Elsevier.

Yim, C., O'Brien, M., McEvoy, N., Winters, S., Mirza, I., Lunney, J. G., & Duesberg, G. S. (2014). Investigation of the optical properties of MoS2 thin films using spectroscopic ellipsometry. *Applied Physics Letters, 104*(10), 103114. doi:10.1063/1.4868108

Youngblood, N., Chen, C., Koester, S. J., & Li, M. (2015). Waveguide-integrated black phosphorus photodetector with high responsivity and low dark current. *Nature Photonics, 9*(4), 247-252. doi:10.1038/nphoton.2015.23

Zhang, H., Ma, Y., Wan, Y., Rong, X., Xie, Z., Wang, W., & Dai, L. (2015). Measuring the refractive index of highly crystalline monolayer MoS2 with high confidence. *Scientific Reports, 5*(1), 8440. doi:10.1038/srep08440

Appendix A

1. 2D Printer Modifications and Optimizations

A new setup was designed for 2D printing using scotch tape exfoliation and microstamping in the previous work by (Hemnani et al., 2018). This setup was used for the transfer of 2D materials on SiP devices. The setup used an electrical probe holder and a needle mounted on an XYZ-direction stage for microstamping of the flakes from PDMS to the devices. As a part of my thesis research, various modifications and optimizations were made to overcome the problems with the setup. These modifications were made to reduce the time required for transferring the materials, ease of use,

repeatability, precise alignment and increasing the probability of transfer. The sections below will be addressing each modification made and the resulting improvements.

1.1 Change in working distance

The working distance in this setup is defined as the distance between the PDMS material and the targeted sample substrate. As we know that PDMS is a stretchable polymer and is very flexible especially for thin layers. The PDMS was mounted on an XYZ-direction stage for aligning the flakes on it with the targeted region. The length of the PDMS kept floating over the sample limited the working distance to be reduced. This was because of the slack formed by the thin PDMS film. If the PDMS was lowered below 1.5-1.8 cm there were high chances that the PDMS might completely stick to the sample substrate leading to transfer of most of the flakes on PDMS on the sample leading to contamination. Another issue being faced was the amount of stretch produced in the PDMS was high while transferring the material flakes by micro stamper as it must travel the working distance to reach the sample. This certainly led to cracking of delicate 2D material flakes as shown in Figure 15. The cracking of flakes was more intense with monolayered or bi-layered 2D materials due to stress and strain subjected during transfer.

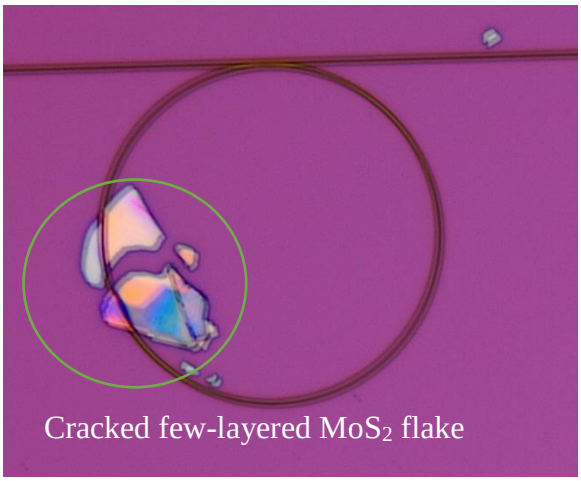

Cracked few-layered MoS_2 flake

Figure 15 Cracking of 2D material flakes

The issue was solved by using a frame made of microscope glass slides such that the PDMS can be clamped between two slides and can be easily mounted on the stage without any expert skills required. The framed helped to reduce the floating area of PDMS over the sample from ~4.5 cm to 1.5 cm. This reduced the slack in the PDMS thus reducing the working distance to few millimeters more than the glass slide thickness. Hence, the effective working distance was ~5-6 mm. This drastic change in working distance reduced the stretching of PDMS to a large extent thus removing the possibility of cracking of flakes due to stress and strain. Figure 16 shows the placement of the frame with the PDMS film on the moving stage. The side view shows the placement of the PDMS close to the sample before transfer after the change in working distance.

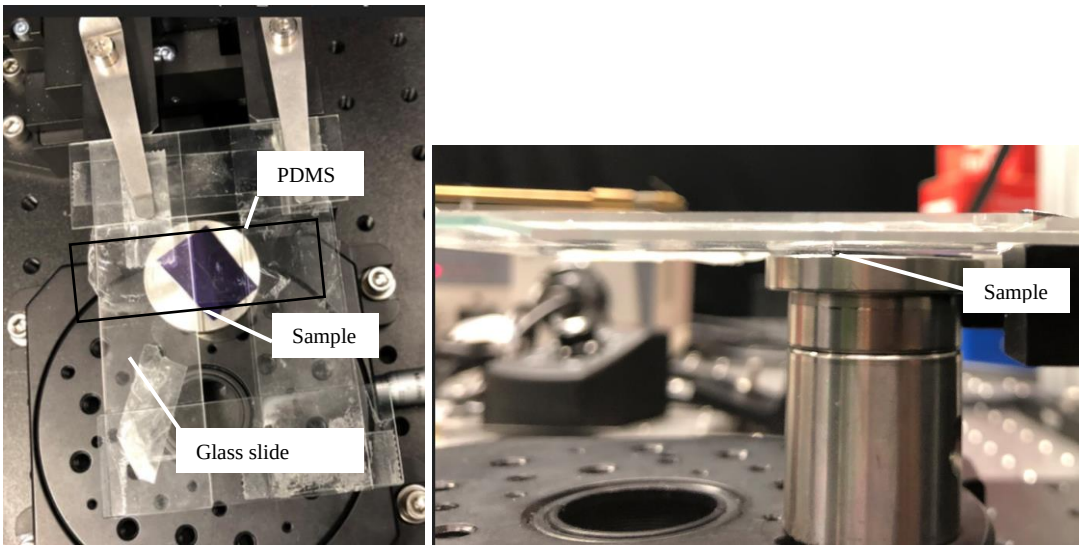

Figure 16 Glass slide frame for holding PDMS and reducing the working distance

1.2 Change in the motion of the needle

The micro stamper was originally held by an electrical probe holder and its knobs were used for moving the needle as shown in Figure 17. The two knobs had a provision to move back and forth both horizontally and vertically. The alignment of the needle during transfer was done by manually moving the holder over the sample as the holder didn't have any x-direction control. Based on this arrangement it was always time-consuming to align the system for accurate transfer of 2D materials over the sample.

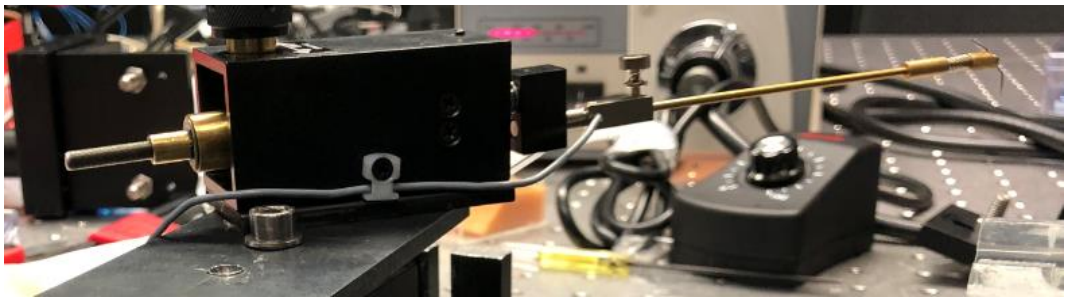

Figure 17 Micro stamper holder fixed on a stationary platform attached by permanent magnets

The vertical movement of the electrical probe holders is designed for an angular movement for better contact with the devices. All the movements in the probe holder are based on spring tension assembly. The length of the arm holding the needle is always made long enough to reach the device from a distance. The electrical probe holder is not meant for linear vertical motion and short arm lengths. Both factors were greatly affecting the performance of the system leading to degradation in accuracy and time required for transfer. The long arm holding the needle acts as a cantilever thus producing random vibrations at micron level while transferring thus leading to target miss. The lack of x-direction control made it troublesome to align the needle over the target. The angular vertical motion helping needle to stamp always caused transfers at random offsets leading to irregularities in estimating the transfer position.

The solution to all the factors required a stable xyz-direction linear stage controller with micro-step control either manual or automatic. Also, a firm needle holder to reduce vibrations during transfers. The new stage installed sufficed the requirements quite well. The vibrations were negligible and within the tolerable levels. The offsets of missing the target during transfer were reduced to ~5 microns. The newly installed stage with a needle holding clip is shown in Figure 18

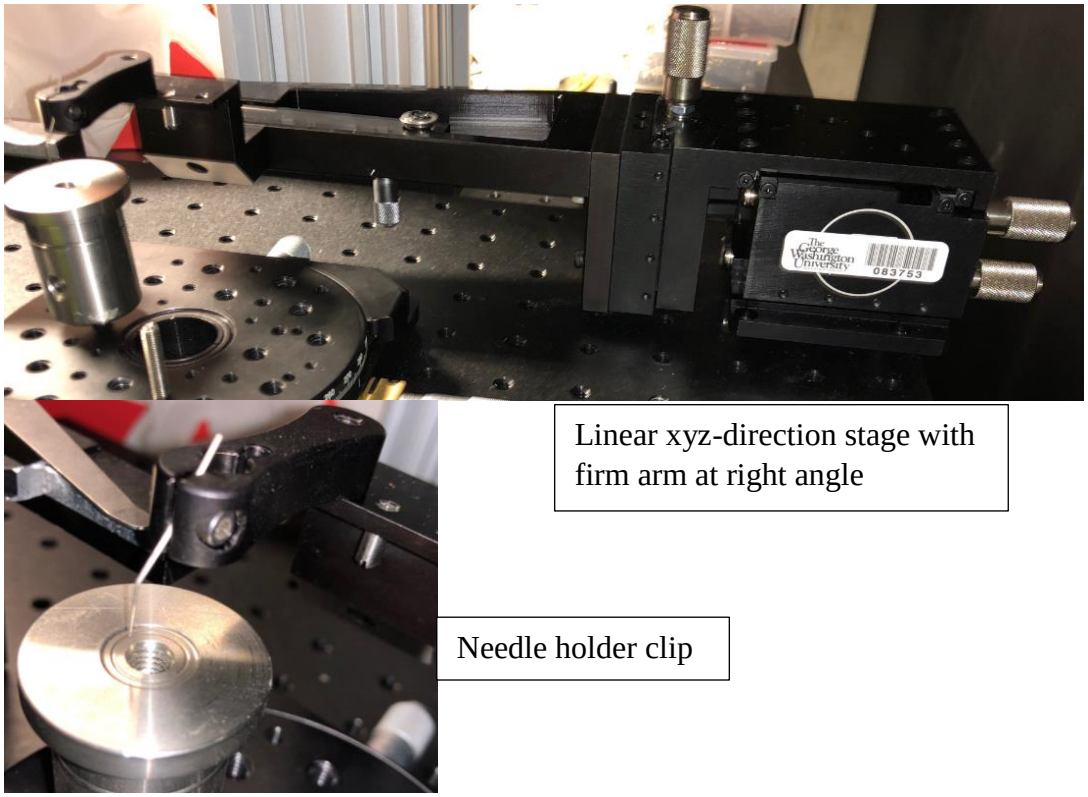

Figure 18 Linear xyz-direction micro-step control stage with the needle holding clip

1.3 Temperature-dependent transfers

There are several different ways and techniques being followed to transfer 2D materials for different research purposes on devices (Hemnani et al., 2018). An extensive study has

been done to enhance the adhesion of 2D materials with different materials. A possible solution is by increasing the temperature of the sample during the transfer process to get rid of the humidity from the surface and help materials to thermally form a stable contact with the sample (Uwanno et al., 2015). While using the 2D printer for a heterogeneous stack of different 2D materials it was experienced that materials like hBN, whose lattice matching abilities are higher leading to strong van der Waals force, the previously transferred material flakes were picked up. The possible reason for this was the humidity on the surface of the sample and irregular surface roughness due to physical exfoliation of the material from bulk.

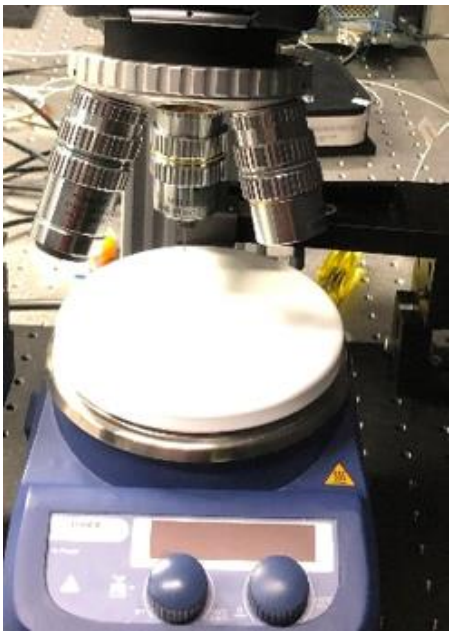

Figure 19 Thermal hot plate introduced in 2D printer

A thermal hot plate was introduced in the 2D printer setup as shown in Figure 19 to make runtime temperature-controlled transfers to increase the adhesion of the flakes with the substrate. Stacking of materials like hBN on hBN, hBN on $MoTe_2$ and only hBn and $MoTe_2$ was performed by varying temperature between 80^{o}C to 120^{o}C as shown in

Figure 20. The transfer was done on a standard SOI substrate. The temperature variation considerably reduced the pressure applied by the micro stamper on the flake during transfer process thus applying less stress on the flake.

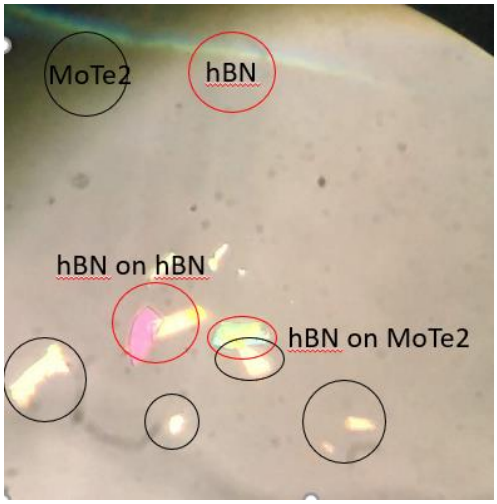

Figure 20 Temperature dependent transfer using a modified 2D printer